JOURNAL OF MATERIALS RESEARCH AND TECHNOLOGY 2023;25:4231–4263

Available online at www.sciencedirect.com

jmr&t Journal of Materials Research and Technology

journal homepage: www.elsevier.com/locate/jmrt

Review Article

Recent advances in Sn-based lead-free solder interconnects for microelectronics packaging: Materials and technologies

T.T. Dele-Afolabi [a,b,*], M.N.M. Ansari [a,**], M.A. Azmah Hanim [c,d], A.A. Oyekanmi [e], O.J. Ojo-Kupoluyi [f], A. Atiqah [g]

[a] Institute of Power Engineering, Universiti Tenaga Nasional, Jalan Ikram UNITEN, 43000, Kajang, Selangor, Malaysia
[b] Department of Mechanical Engineering, Faculty of Engineering, Ajayi Crowther University, P.M.B. 1066, Oyo, Oyo State, Nigeria
[c] Department of Mechanical and Manufacturing Engineering, Faculty of Engineering, Universiti Putra Malaysia, 43400, UPM Serdang Selangor, Malaysia
[d] Advance Engineering Materials and Composites Research Center, (AEMC), Faculty of Engineering, Universiti Putra Malaysia, 43400, UPM Serdang Selangor, Malaysia
[e] Institute of Energy Infrastructure (IEI), Universiti Tenaga Nasional, Jalan Ikram UNITEN, 43000, Kajang, Selangor, Malaysia
[f] Department of Sugar Engineering, Nigeria Sugar Institute, Km.18, Ilorin-Kabba Highway, Ilorin, Nigeria
[g] Institute of Microengineering and Nanoelectronics, Universiti Kebangsaan Malaysia, 43600, Bangi, Selangor, Malaysia

ARTICLE INFO

Article history:
Received 21 April 2023
Accepted 20 June 2023
Available online 25 June 2023

Keywords:
Sn-based solder
Intermetallic compounds
Interlayer components
ENImAg surface finish
Rotary magnetic field
Energy

ABSTRACT

The electronic industry faces a number of issues as a result of the rapid miniaturization of electronic products and the expansion of application areas, with the reliability of electronic packaging materials playing a significant role. Moreover, the continuously harsh service conditions of electronic products like high current density and excessive Joule heat will lead to severe reliability concerns of electromigration and thermomigration, which evidently curtail the lifespan of solder joints. Therefore, to maintain the reliability of solder joints in recent microelectronic applications, several investigations have been conducted in the last decade to proffer solutions to the drawbacks affecting the full implementation of the Sn-based solders in advanced packaging technologies. This article reviews the recent developments on the reliability investigation of Sn-based solder joints and discusses the influence of interlayer materials, electroless nickel immersion silver (ENImAg) surface finish, geopolymer ceramics and rotary magnetic field (RMF) technology. The 3D network structure of porous interlayer metals and the beneficial features of ENImAg surface finish have demonstrated to be highly efficient in revamping existing lead-free solders by satisfying the needs of both high-temperature service operation and low-temperature

* Corresponding author. Institute of Power Engineering, Universiti Tenaga Nasional, Jalan Ikram UNITEN, 43000, Kajang, Selangor, Malaysia.
** Corresponding author.
E-mail addresses: temitope@uniten.edu.my (T.T. Dele-Afolabi), ansari@uniten.edu.my (M.N.M. Ansari).
https://doi.org/10.1016/j.jmrt.2023.06.193
2238-7854/© 2023 The Authors. Published by Elsevier B.V. This is an open access article under the CC BY-NC-ND license (http://creativecommons.org/licenses/by-nc-nd/4.0/).

soldering. While transient current bonding technology is efficient at preventing agglomeration and floating of nano-sized reinforcements in composite solders, RMF technology is effective in controlling the flow and solidification of liquid metal during the soldering process. Finally, emerging technologies for future research directions have been summarized to provide further theoretical basis required for the investigation of solder joint reliability of electronic devices in service.
© 2023 The Authors. Published by Elsevier B.V. This is an open access article under the CC BY-NC-ND license (http://creativecommons.org/licenses/by-nc-nd/4.0/).

1. Introduction

Bonding technology is of utmost importance in microelectronic packaging since it allows mechanical and electrical interconnection between the semiconductor chips and the printed circuit board. Function integration and downsizing of electronic devices have become essential trends that call for better dependability of solder joints as the electronic industry experiences rapid technological improvement [1–5]. Solder alloy as the major material that forms the solder joint has been utilized in surface mount technology (SMT), ball grid array (BGA) and chip-scale package (CSP) for microelectronic packaging [6–8]. Hence, solder performance plays a pivotal role in the reliability of the solder joint [9].

Even though, the Sn–Pb solders have advantages in low melting temperature, affordability and excellent wettability [10,11], given the RoHS (Restriction of Hazardous Substances) Act [12,13], and the increased sensitivity on green electronic packaging [14], the industry is compelled to rule out the utilization of Pb-based solders [15]. Given this circumstance, the Pb-free solder alloys, most especially, the Sn-based solders (e.g. SnBi, SnAg, SnCu and SnAgCu) have been widely researched and employed in soldering applications [16–20]. Nevertheless, the Sn-based solders are affected by limitations generated by elevated thermal stress and evolution of thicker interfacial IMCs, which give rise to issues over their reliability, especially in application areas involving harsh operating conditions [21–24].

More specifically, the introduction of alloying elements [25–27], especially micro/nanoparticles including carbon nanotubes and graphene nanosheets [28–33] to Sn-based solder has been employed to impede the excessive evolution of IMCs in the course of aging and enhance the mechanical properties of the solder joint. Additionally, it has been demonstrated that adding nanoceramics such as nano-TiN particles to lead-free solder systems can improve the wettability, microstructural refinement, and mechanical properties of the solder joints [34]. However, these approaches cannot efficiently control the development of composite solders with homogenous composition that will result to irregular thickening of the interfacial IMCs in few locations at the solder/substrate interface. Therefore, appreciable microstructural optimization is required to further improve the solder joint performance.

In recent times, interlayer metals with a continuous 3D structure have been applied in the field of electronic packaging owing to their remarkable mechanical properties, thermal conductivity and electrical conductivity [35,36]. The potentials of these interlayer metals as viable reinforcements for lead-free solder joints have been demonstrated in recent studies [37,38]. Besides, the surface technology for the production of printed circuit board (PCB) offers enhanced solder joint reliability [39–43]. Among the surface finishes employed to date, the ENImAg is no doubt an economically viable candidate with the capacity for the reliability enhancement of various solder materials [44,45]. More so, investigations conducted recently have showcased high-performance geopolymer ceramics comprising a semi-crystalline structure with Si–O–Al and Si–O–Si bonds as viable materials for the development of high-performance composite solders [46–50].

Most recent, microstructural modification and mechanical performance enhancement of solder alloys have been achieved by applying electromagnetic field during the course of solidification [51–53]. As numerous published review papers [54–59] have already focused on the alteration of the Pb-free solder materials through doping with micro- and nano-sized articles, this study creates a holistic insight into the recent developments in the last decade for revamping existing Sn-based solders. The influence of interlayer metals, ENImAg surface finish, geopolymer ceramics and rotary electromagnetic field on the wettability, melting temperature, microstructure and mechanical behavior of different Sn-based solder systems are comprehensively discussed (see Fig. 1).

There are eight sections in this article. In section 2, the survey methodology is described. The various interlayer components including porous copper, nickel foam and others are highlighted in Section 3. In Section 4, significant improvement in the overall reliability of Sn-based solder joints using the ENImAg surface finish is reported. The beneficial effects of geopolymer ceramics addition to Sn-based solder systems are described in Section 5. Section 6 reviews the rotary magnetic field technology and the joint reliability enhancement of Sn-based solders from the perspectives of flow and solidification behaviour of molten solder during the soldering process. In Section 7, some emerging technologies that have proven to be beneficial to the microelectronics packaging industry have been put forward for more comprehensive research and evaluation. Finally, the article ends with the concluding remarks in Section 8.

2. Survey methodology

The preferred reporting items for systematic review and meta-analysis (PRISMA) procedure [60] was used in this study

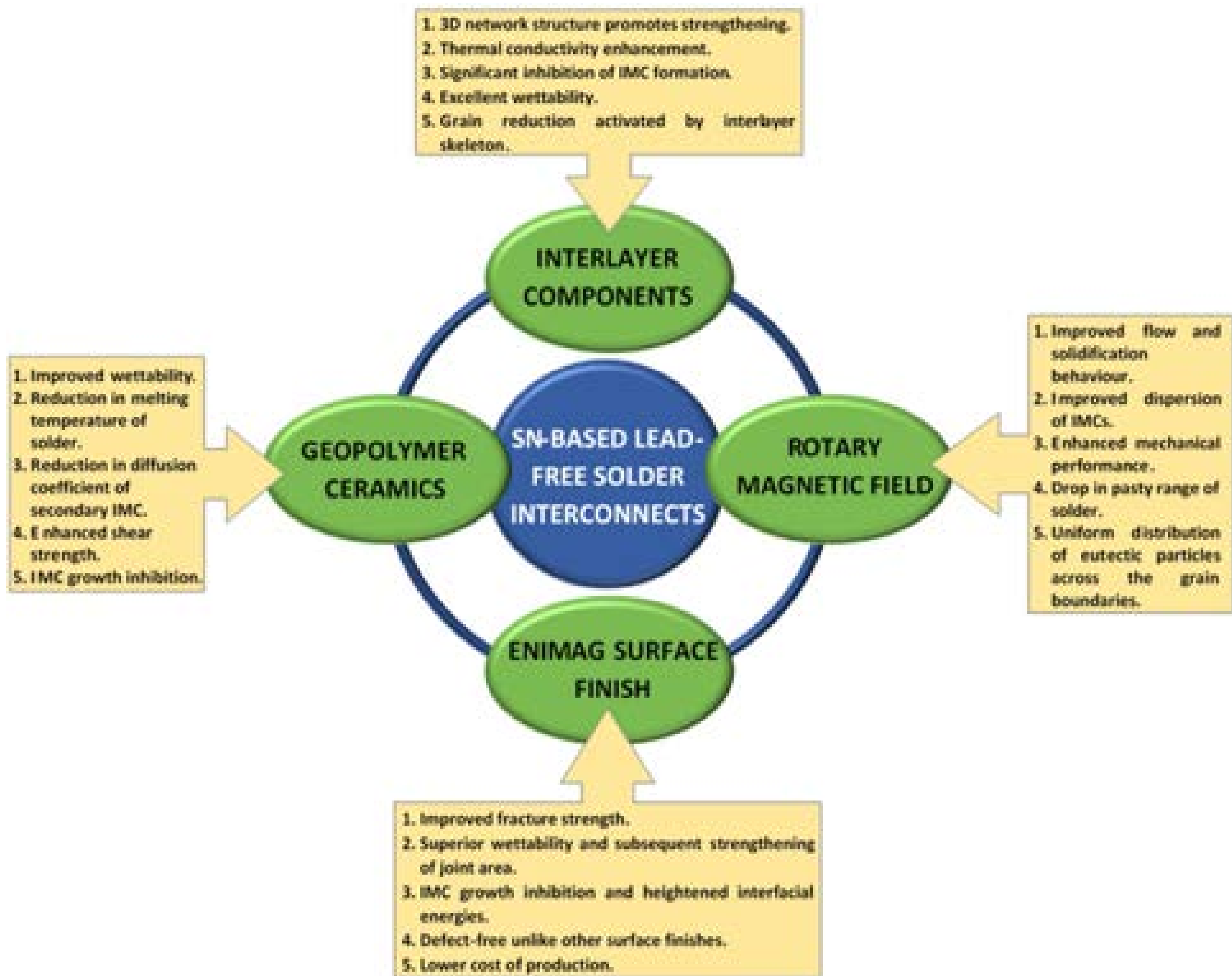

Fig. 1 – Schematic summary of recent materials and technologies for enhancing the reliability of Sn-based solder joints.

to conduct the literature search. Scopus, ScienceDirect, and IEEE Xplore were just a few of the well-known databases used to search for the relevant papers. Accordingly, it was discovered that 2669 papers had been published within the last decade on the three databases that were emphasized. Using the procedure shown in Fig. 2, 144 highly relevant publications were chosen for in-depth research after the authors conducted rigorous screening and investigation. The final 144 articles were organized into five themes: interlayer components, electroless nickel immersion silver surface finish, geopolymer ceramics, rotary magnetic field and emerging technologies for solder joint reliability enhancement. To create the background, contributions, and application of the analysis, 204 papers altogether deemed closely related to the study's focus were looked into and incorporated in other sections of the paper.

3. Interlayer components

Interlayer materials with 3D continuous network structure have wide application in petrochemical, aerospace, energy industry and other areas owing to their inherent properties including excellent thermal property, light weight and improved ductility [61–63]. Based on their compositions, porous metals are often categorized into the single composition metal foams such as copper foam [64–66], nickel foam [67–69], aluminum foam [70,71] and compound composition type like FeCrAl [72,73] foam. Recently, porous metals have been investigated as promising reinforcements to enhance the performance of bonding layers. In the field of metal joining, the unique 3D structure of porous Cu facilitates improved interfacial behavior during diffusion bonding [74,75], high efficiency of heat transfer for relieving CTE mismatch-influenced residual thermal stress [76,77] and remarkable absorption of energy through plastic deformation [78,79].

3.1. *Porous copper*

The effect of porous Cu (1 mm thick) additions of 100 pores per inch (pore size = 0.2 mm) and 500 pores per inch (pore size = 0.05 mm) (Fig. 3a and b) on the microstructure (Fig. 3c and d), mechanical and thermal properties of SnBi/Cu solder joint was reported by Liu et al. [80,81]. The introduction of the porous Cu led to hardness enhancement of the Bi-rich and β-

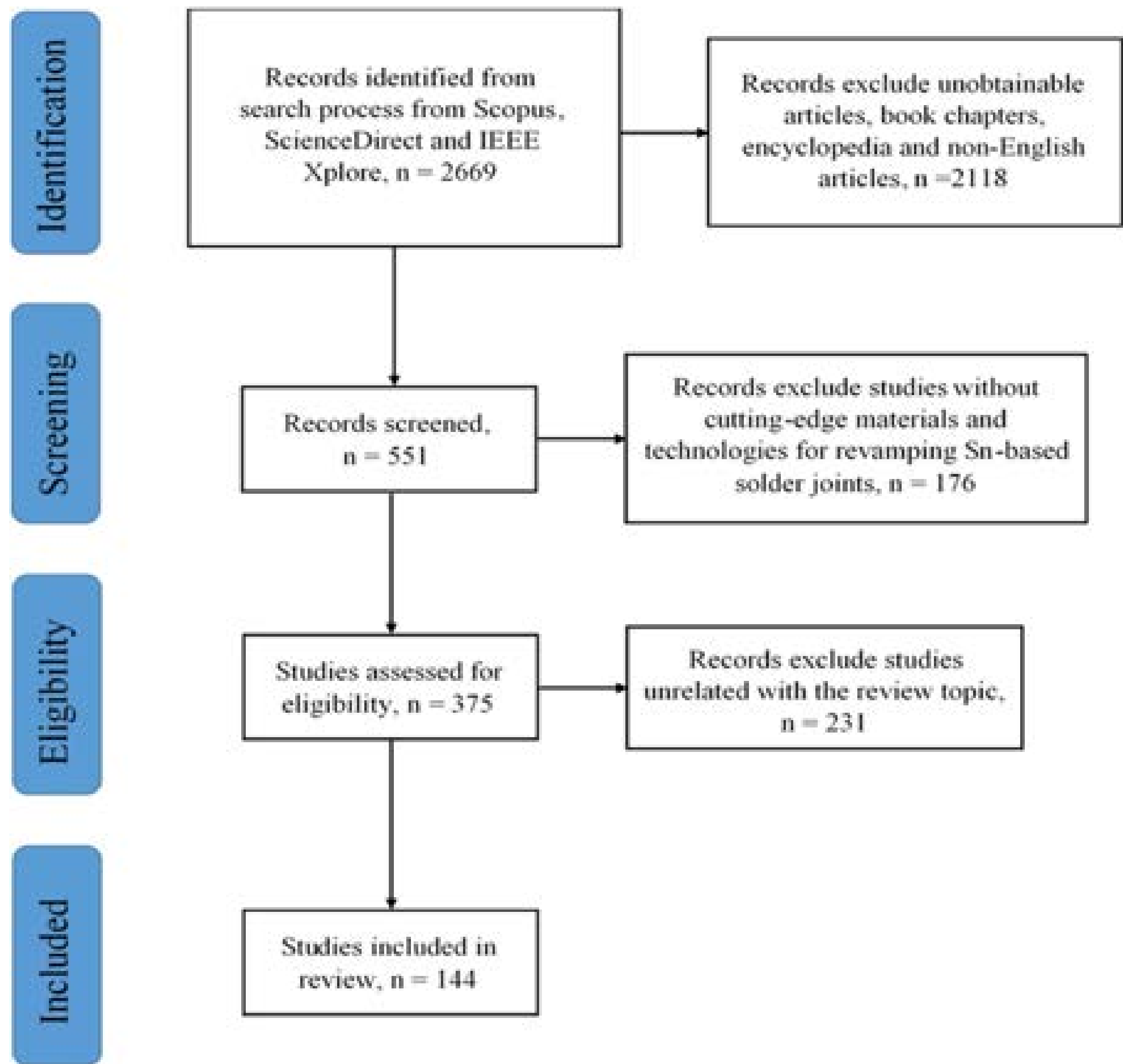

Fig. 2 – PRISMA-based literature selection methodology.

Sn phases present in the SnBi solder. From the morphology of the IMC layer, it was observed that the IMC grain size increased in both solders enhanced with porous Cu and consequently resulted in thicker IMC layers relative to the SnBi/Cu counterpart. This occurrence is mostly due to an increase in the Cu content of the solder caused by the inclusion of porous Cu. Porous Cu and molten solder interact during the soldering process to produce a reaction where Cu atoms disperse into the liquid solder and migrate along with the solder's internal motion. This phenomenon raises the concentration of Cu atoms at the solder/substrate interface, which in turn favours the development of the Cu_6Sn_5 IMC.

As a result of the porous Cu interlayer's inclusion, thermal conductivity values of the solder alloy increased remarkably (Fig. 3e) due to the relatively high thermal conductivity of Cu (398 W/mK). A comparison between the SnBi and SnBi@P–Cu showed that porous Cu incorporation actuated the formation of a localized ring-shaped Cu pattern within the solder. Notably, the thermal conductivity of the SnBi@500P–Cu is higher in comparison to its SnBi@110P–Cu counterpart due to the higher content of Cu which was effective in facilitating heat transfer via the porous Cu's array structure. Adding to the aforementioned conclusions, the impact of isothermal aging on the development of the interfacial IMC layer in the porous Cu-reinforced SnBi solder alloy was reported [82]. After 21 days of aging at 100 °C, the solder joints with porous Cu additions exhibited lesser IMC layer thicknesses in comparison to the SnBi/Cu counterpart. This was further substantiated with the growth rates estimated from the empirical diffusion formula of 0.61506 μm/day$^{1/2}$, 0.48725 μm/day$^{1/2}$ and 0.55385 μm/day$^{1/2}$ for SnBi/Cu, SnBi@110P–Cu/Cu and SnBi@500P–Cu/Cu, respectively (Fig. 1f).

Incorporating porous Cu (1 mm thick) with a pore size of 1.3 mm into SnBi–Ag solder matrix also improved the microstructure and strength of the solder interconnects [83].

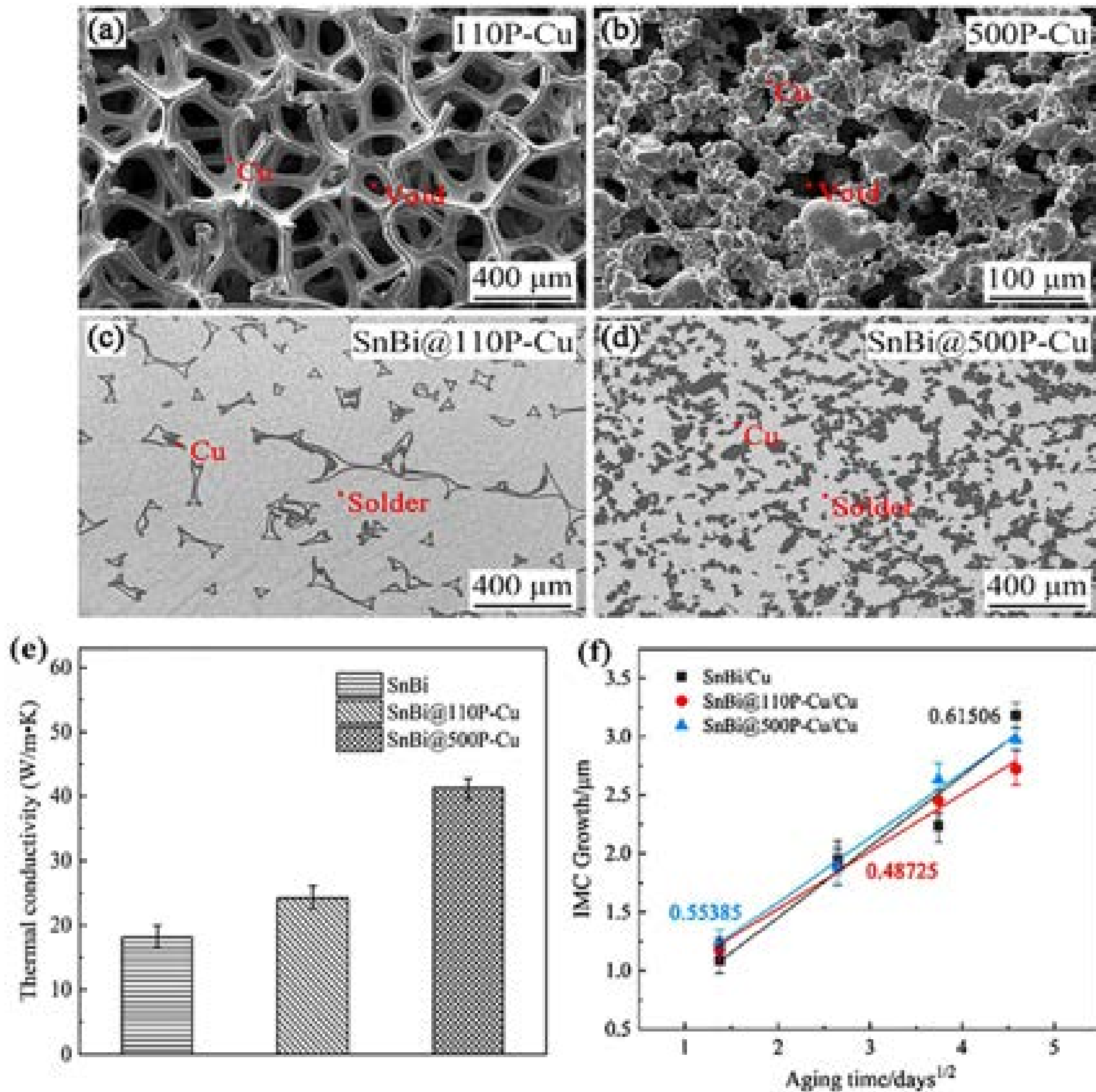

Fig. 3 – Microstructures of the porous Cu sheets of (a) 110 PPI, (b) 500 PPI, and solder sheets for (c) SnBi@110P–Cu, (d) SnBi@500P–Cu, (e) thermal conductivity plot of the SnBi@xP-Cu, and (f) correlation between IMC growth and square root of aging duration [80,82].

In the SnBi-xAg matrix, multiple triangular spots surrounded by porous Cu frames were formed due to the presence of porous Cu. The porous Cu frames inhibited the growth of both the Bi-rich and β-Sn phases in these locations leading to remarkable microstructural refinement inside the triangular spots. As a result, the degree of hardness in the porous Cu frame sections was significantly enhanced as compared with that of the surrounding solder bulk. More so, the introduction of porous Cu led to improved shear strength, particularly the SnBi-0.4Ag@P-Cu solder joint which exhibited the superior shear strength.

The microstructure of porous Cu was barely effective on the IMC morphologies of the SnBi@P–Cu/Cu, SnBi-0.4Ag@P-Cu/Cu and SnBi–1Ag@P–Cu/Cu solder joints [84]. Nevertheless, because the solder bulks contained more Cu than usual, the interfacial IMCs exhibited slight growth. Meanwhile, porous Cu addition showed no remarkable impact on the IMC evolution of the solder joints, most especially the SnBi-xAg samples subjected to isothermal aging (Fig. 4a). Besides the strength improvement before and after aging actuated by the addition of Ag particles to the SnBi matrix, it was found that the shear strength before and after aging was further enhanced by the inclusion of porous Cu to the solder joints. (Fig. 4b). Porous Cu dispersed in the solder matrix to promote dispersion strengthening and the resulting skeleton of porous Cu exhibited capacity for crack propagation inhibition during shear test. Hence, the synergetic shear strength improvement of the solder joint. In the same vein, porous Cu was effective in improving hardness at regions within the porous Cu frame (see region a; Fig. 4c). The quantitative effect can be observed in the higher hardness exhibited by the ‘region a’ for the three solder joints tested relative to ‘region b’

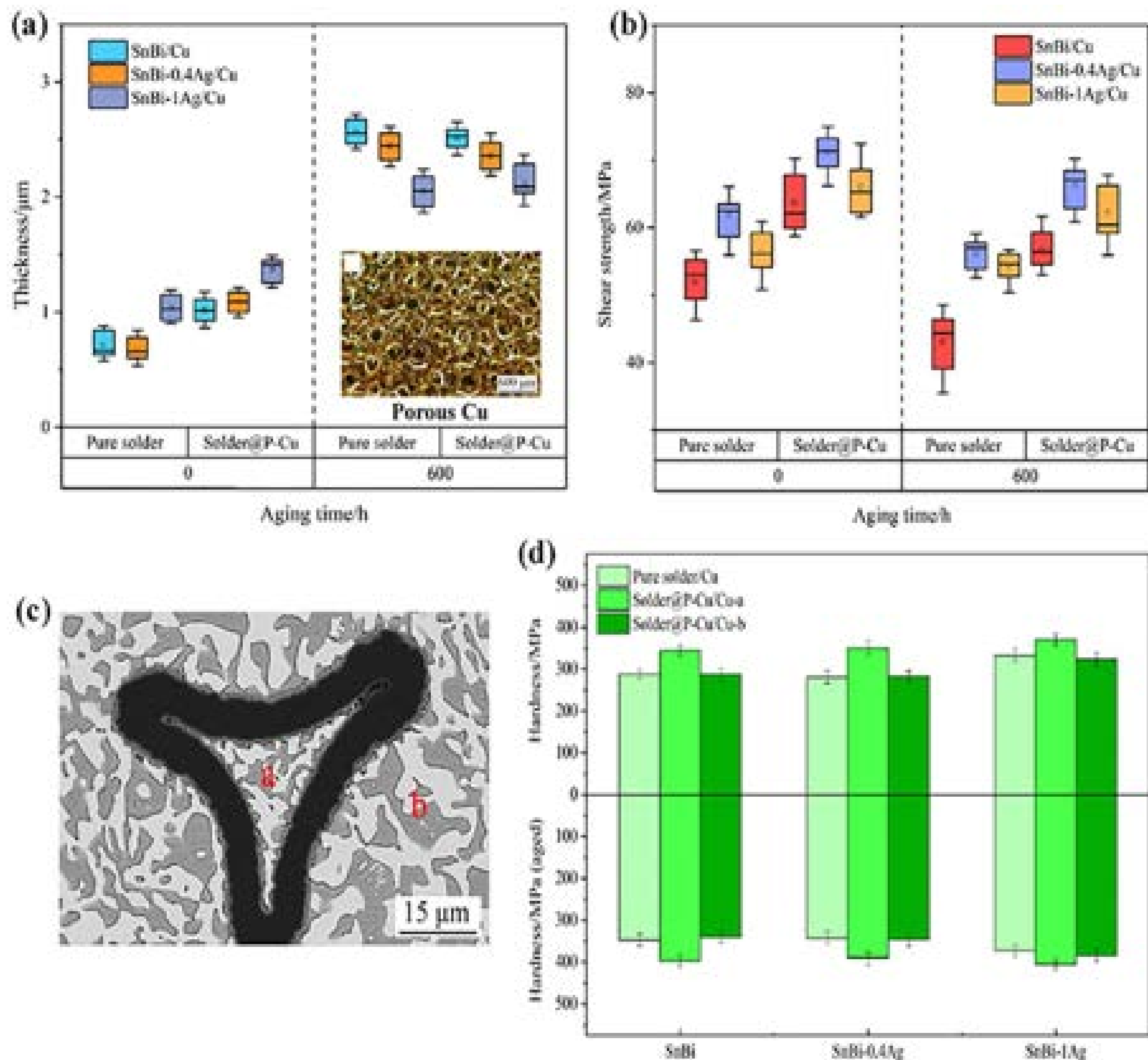

Fig. 4 – (a) Interfacial IMC thickness values and (b) shear strength values of the solder joints against the aging time; (c) microstructure of SnBi-0.4Ag solder bulk, (d) hardness of SnBi-xAg solder bulks [84].

(Fig. 4d). The existence of refined microstructure in this region was attributed to this finding.

To avoid the poor contact between porous Cu and the Cu board during reflow soldering process due to the lower specific gravity of porous Cu, pressure aided soldering of Cu using porous Cu-reinforced Sn58Bi solder was employed elsewhere [85]. The sizes of the pores for the 100 PPI and 500 PPI are 200 μm and 50 μm, respectively, while the thicknesses of the struts are 1.3 mm and 1.0 mm. The soldering process involves preparing a sandwich structure with SnBi@porous Cu composite interlayers (100 PPI and 500 PPI) pressed in between two Cu substrates at 180 °C, under 0.1 MPa for 3 min. From the examined microstructures (Fig. 5), the SnBi@500P–Cu/Cu exhibited more porous Cu skeletons and very few solder portion within the solder bulk in comparison to the SnBi@110P–Cu/Cu. With this microstructure, the reliability of the SnBi solder joint can be enhanced to meet the conditions for low-temperature soldering and high-temperature operating condition. Meanwhile, the shear strength of the SnBi@110P–Cu/Cu exhibited the highest strength relative to other solder joints. The result was supported with the different fracture morphologies exhibited by the solder joints reinforced with porous Cu and the plain counterpart where fracture mainly occurred in the solder bulk of the SnBi@xP-Cu relative to the brittle interfacial fracture associated with the SnBi solder joint.

Elsewhere [86–88], the joint strength of SAC 305/Cu joint reinforced with 15 PPI (Ø = 1.7 mm) and 25 PPI (Ø = 1.0 mm) porous Cu interlayers with 0.1 mm thickness increased as the soldering duration and temperature were sequentially increased. The typical fracture in between the solder and Cu board was exhibited by the solder joint without porous Cu whereas, the solder joints with porous Cu fractured at three regions, including the solder/porous Cu interface, the interior of porous Cu and within the solder. Also noticeable was the fact that the IMC was thicker at the interface of the solder and

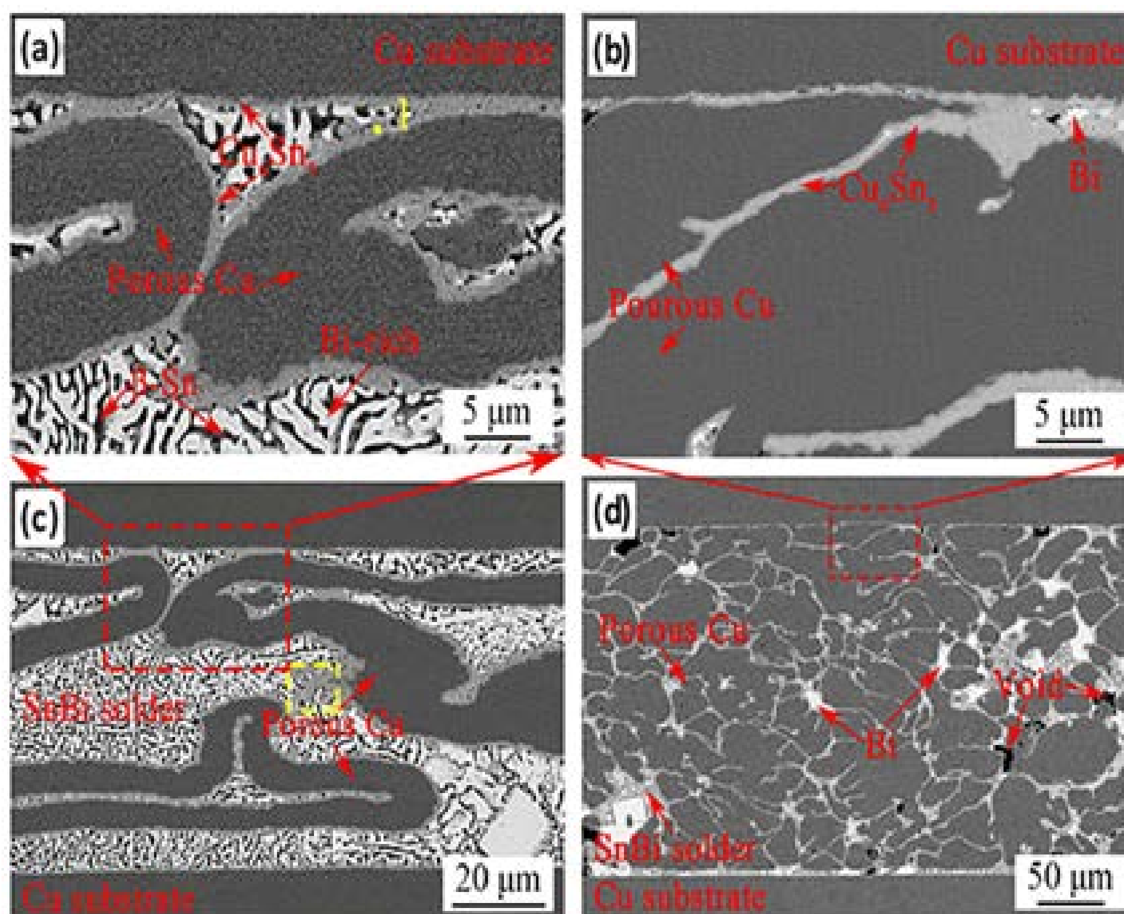

Fig. 5 – Magnified microstructures of (a) SnBi@110P–Cu/Cu, and (b) SnBi@500P–Cu/Cu; microstructure of (c) SnBi@110P–Cu/Cu, and (d) SnBi@500P–Cu/Cu [85].

Cu board relative to the solder/porous Cu interface. The substantiating phenomenon is the irregular area of contact at the solder/porous Cu interface which led to the less intense IMC layer formation. Upon subjecting similar set of samples to isothermal aging at 150 °C and aging duration between 100 and 500 h, the joint strength deteriorated with increased isothermal aging duration as expected and crack initiation occurred mainly at the interfaces between the SAC 305 and porous Cu [89].

The P35 porous Cu with a uniform thickness of 0.1 mm was introduced in addition to those used above by the similar authors for the purpose of further showcasing the porous Cu interlayer as a viable component in enhancing solder joint reliability [90]. A thinner solder layer was noticed in the soldered sample having the P15 porous Cu due to the relatively easy penetration of the liquid solder through the larger pores. However, samples prepared with both the P25 and P35 porous Cu exhibited thicker solder layer of approximately 80 μm since the liquid solder was unable to easily penetrate through the smaller pores present in these grades of porous Cu interlayer. Meanwhile, it was noticed that the IMC grew thicker with rising pore size of the porous Cu component indicating the difficulty in molten solder penetration with increasing pore size and the subsequent solidification at the porous Cu-solder alloy interface. Findings reported regarding how cooling rate affects the IMC layer thickness revealed that the smaller pore sizes of the P25 and P35 resulted in prolonged cooling duration for solder solidification in comparison to the P15. The gradual cooling rates demonstrated by the samples with P25 and P35 increased the time for Cu_6Sn_5 growth and formation at the interface layer of liquid solder.

Comparative investigation on the evolution of IMC layer and shear strength behavior of MWCNTs-doped SAC 305 composite solders incorporated with porous Cu (15, 25 and 50 PPI) was systematically performed by Hanim et al. [91]. Prior to the soldering process, the porous Cu materials were rolled to achieve homogenous layer and to reduce the gap formed in the resultant joint. The average sizes of the pores for the 15, 25 and 50 PPI are 0.68 mm, 0.29 mm and 0.14 mm, respectively, while in a similar sequence, the average thicknesses of the struts are 0.17 mm, 0.06 mm and 0.03 mm. The porous Cu materials were more effective in inhibiting the IMC growth at the interfaces of both the solder/Cu and the solder/porous Cu for the solder doped with 0.01 wt% MWCNTs as compared with the 0.04 wt% MWCNTs counterpart.

Better MWCNTs dispersion was observed in the SAC solder/porous Cu doped with 0.01 wt% MWCNTs as compared with the counterpart with 0.01 wt% MWCNTs which led to the enhancement in retardation of the active Sn atoms and a concurrent retardation in the accelerated dissolution of Cu

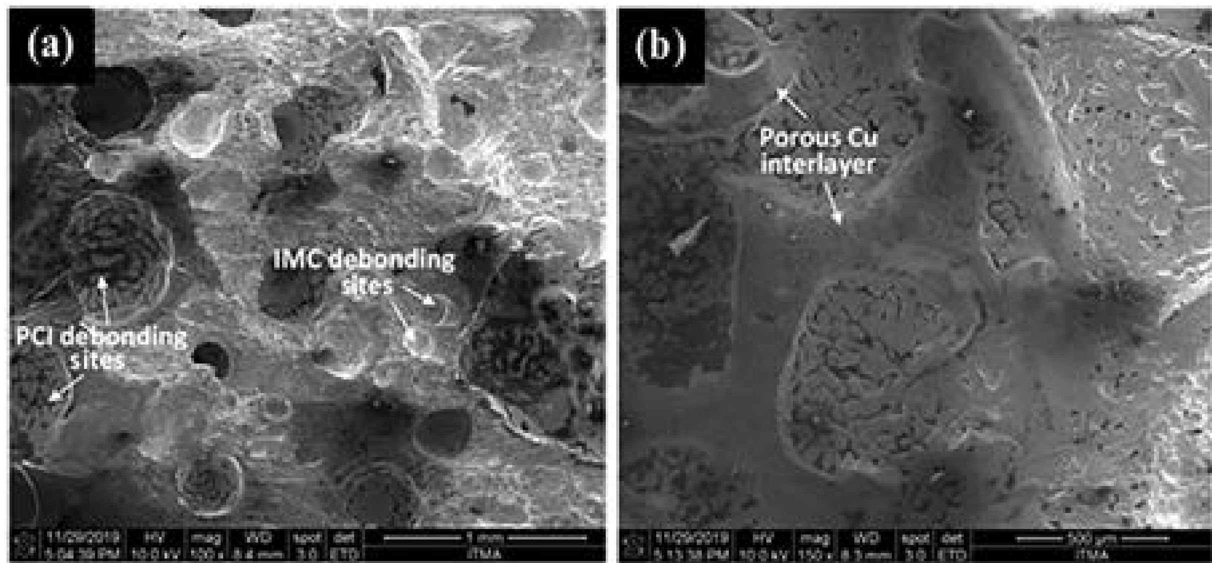

Fig. 6 – Microstructures of the disconnected Cu substrates from the fractured (a,b) SAC-0.01CNT-15PCI [91].

atoms at the interfaces of both the solder/Cu and the solder/porous Cu for the formation of IMC layer. In addition, the porous Cu materials were highly influential in enhancing the shear strength of the MWCNTs-doped SAC 305 solder joint, particularly solder joints reinforced with 0.01 wt% MWCNTs. From the fracture surfaces (Fig. 6) of the disconnected Cu substrates from the failed single-lap joint, it was surmised that fracture mostly occurred at the solder/porous Cu interface, where the highly ductile porous Cu was able to reduce stress.

By employing different Cu-foams of 0.15 mm and 0.5 mm thicknesses as reinforcing structures, a strong metallurgical bond was formed between the Cu board and Cu-foam/SAC305 layer with no presence of cracks [92]. Under the joint influence of Cu-foam and ultrasonic vibration, the study revealed a novel technique for the design and fabrication of solder interconnects with the highest reliability in microelectronic applications. By extending the ultrasonic soldering duration to 30 s, the Cu skeleton was largely liquefied in the SAC305, and the Cu_6Sn_5 IMC was detached from the subsequent IMC layer and broken into microscopic proportions by applying the ultrasonic vibration. Meanwhile, the 3D repeated network structure of Cu-foam alongside microstructure refinement actuated by ultrasonic cavitation synergistically enhanced the shear strength of the SAC305 solder interconnect.

The lotus porous Cu having tubular pores (Ø = 174 μm) arrayed in a particular direction (Fig. 7a) was bonded to Cu substrate utilizing the SAC305 solder under diverse bonding modes and diverse orientations in the lotus porous Cu [93]. Three kinds of bonding modes were employed in the study including; (i) mode 1, where the interface of the joint is normal to the direction of pores of the lotus porous Cu and (ii) mode 2 and mode 3, where direction of pores is parallel to the joint interface. The shear strength analysis revealed that even though the bonding regions of the entire lotus porous Cu joints were more expansive relative to the nonporous Cu joint, the entire lotus porous Cu joints demonstrated inferior joint strengths relative to that of nonporous Cu joint (Fig. 7b). Nevertheless, the bonding ductility of the entire porous Cu joints was enhanced relative to the nonporous Cu counterpart.

The entire lotus type porous Cu joints showed high von Misses stresses at the two extremes of a pore located on the lotus porous Cu/solder interface, according to a simulation using the Finite Element Analysis (FEA) on the stress distribution of soldered interconnect under shear stress. (Fig. 7d–f). More so, von Misses stress was large at the LHS of the Cu substrate/solder interface of the same set of samples. The maximum von Misses stress of these samples was comparatively higher than that of the nonporous counterpart (Fig. 7c). It was inferred that the deformation of pores in lotus porous Cu probably occurred as a result of stress concentration around pore structures in the course of the shear test. Hence, the shear strength deterioration demonstrated by the lotus-type porous Cu joints was attributed to the debonding between the pore wall and solder interface by pore distortion in the course of the shear strength investigation.

Nanoporous Cu (NPC) sheet having uniform ligament-pore microstructure (mean pore size 320 nm) was prepared by dealloying $Cu_{40}Al_{60}$ precursor alloy in 1.45 mol/L HCl solution and later sandwiched two Cu substrates with infiltrated SAC 305 solder [94]. A high-temperature resistant bondline was created as a result of the NPC's excellent solder wettability on both the inner and outside components. The average shear strength of these bondlines was 37.68 MPa while the highest shear strength got up to 57.38 MPa. Moreover, the mean resistivity demonstrated by the bondlines was 13.38 μΩ cm. More so, the bondlines exhibited no clear defect after aging at 200 °C for 360 h. Hence, the bondlines were not significantly degraded in terms of the Vickers hardness and shear strength properties after the aging process.

Koga et al. [95] investigated the structure of a fabricated nanoporous Cu sheet and the shear strength of the resultant joint utilizing the NPC sheet to affirm its suitability for high-temperature application. The bonded area produced by utilizing the NPC sheet was performed on an electroless nickel

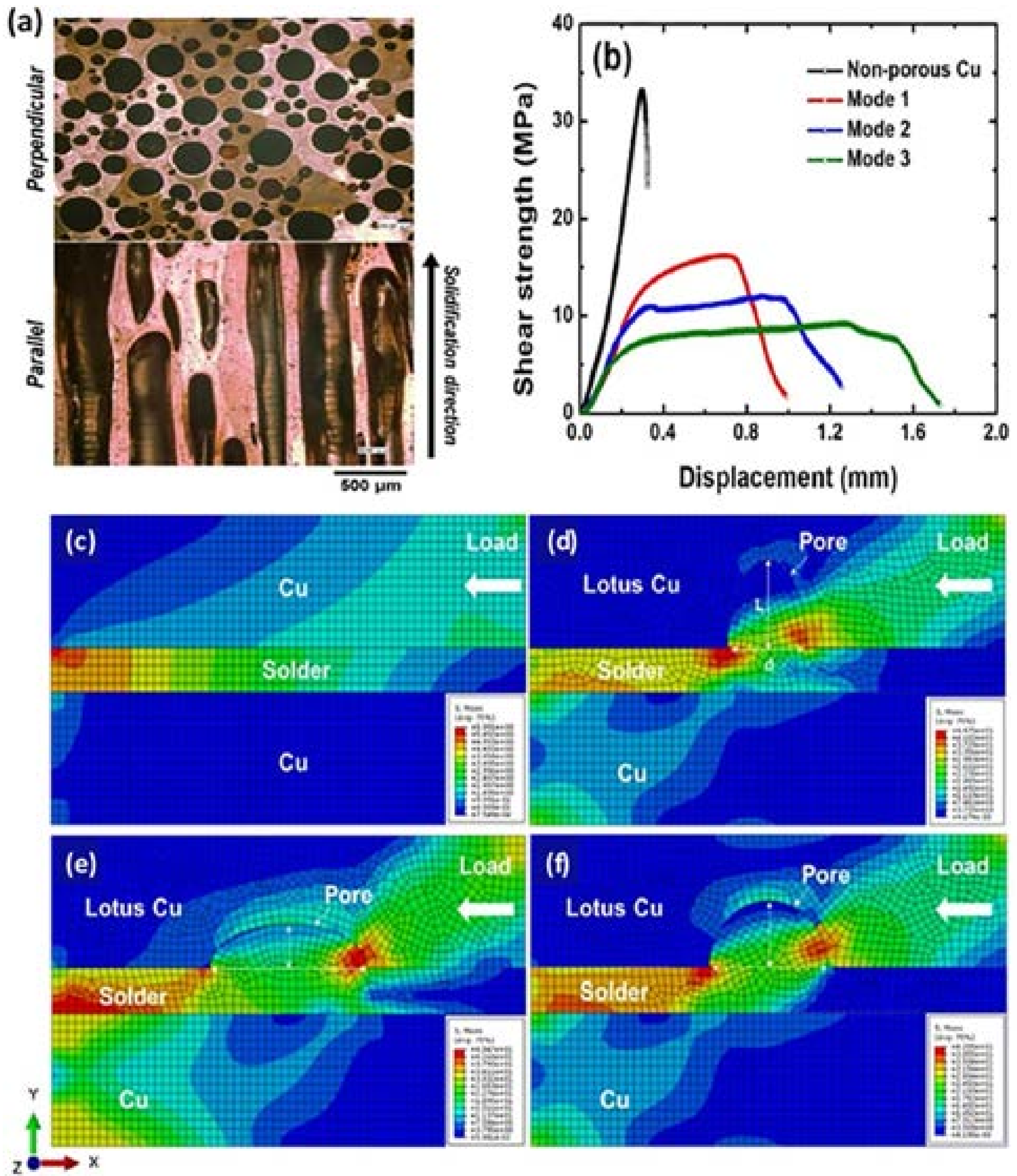

Fig. 7 – (a) Cross-sectional views of lotus porous Cu, (b) shear strength versus displacement plots of joints with diverse bonding modes, stress distribution of (c) nonporous Cu joint and lotus type porous Cu joints for (d) mode 1, (e) mode 2, and (f) mode 3 during the shear strength investigation [93].

immersion gold (ENIG) substrate. With the spontaneous reaction between the surface structure of NPC and the Au from the substrate, the shear strength of the joint prepared with NPC sheet was seven times higher than the joint with no NPC sheet.

Table 1 summarizes the various solder reliability improvements actuated by the reinforcement of traditional and composite lead-free solders with porous Cu interlayer. Clearly from the highlighted studies, porous Cu demonstrated immense capacity in revamping existing lead-free solder interconnects.

Table 1 – The effect of porous Cu on the solder reliability of lead-free solder joints.

Solder material	Solder reliability improvement	Ref.
Sn–58Bi	Hardness enhancement was achieved in the Bi-rich and β-Sn and thermal conductivity of the solder increased with porous Cu incorporation.	[80,81]
Sn–58Bi	Effect of isothermal aging was minimal on the IMC layer thickness and the growth kinetics of the IMC.	[82]
Sn–58Bi-xAg (x = 0.4–1 wt%)	Porous Cu addition strengthened the solder and demonstrated capacity for crack propagation inhibition during shear test.	[83,84]
Sn–58Bi	The brittle interfacial fracture of the plain solder joint was transformed into fracture within the solder bulk for the porous Cu reinforced solder which led to the superior shear strength of the porous Cu reinforced Sn–58Bi solder.	[85]
SAC 305	IMC layer grew thicker with increasing pore size of porous Cu interlayer indicating difficulty in molten solder penetration with rising pore size and the addition of porous Cu with smaller pore sizes led to prolonged cooling period for solder solidification.	[90]
SAC305-xMWCNTs (x = 0.01–0.04 wt%)	The porous Cu was more capable of inhibiting the interfacial IMC layer growth and enhancing the solder strength with 0.01 wt% MWCNTs addition as compared with the 0.04 wt% MWCNTs counterpart.	[91]
SAC305	The 3D repeated network structure of Cu foam together with the grain refinement actuated by ultrasonic cavitation synergistically enhanced the shear strength of the solder joint.	[92]
SAC305	Despite the lower shear strength of the lotus porous Cu solder joints and with the supporting von Misses stresses demonstrate by these joints relative to the nonporous Cu solder joint, the lotus porous Cu solder joints demonstrated superior bonding ductility.	[93]
SAC305	Excellent wettability of the solder on the nanoporous Cu led to the development of a high-temperature resistant bondline with maximum shear strength of 57.38 MPa and mean resistivity of 13.38 μΩ cm.	[94]

With the 3D continuous network structure of the porous Cu, microstructural refinement was achieved which subsequently led to significant strength enhancement of the solder joints. More so, the observed improvement was substantiated using the fracture morphologies of the tested samples wherein fracture occurred primarily in the bulk of the solder joint reinforced with porous Cu as compared with the brittle interfacial fracture associated with the plain counterpart.

3.2. *Nickel foam*

Open cell Ni-foam having remarkable mechanical properties and excellent metallurgical reactivity has shown great potentials as a strengthening component in solder materials. He et al. [96] carried out a comparative research on the microstructural and mechanical properties of Sn-based composite solders reinforced with three distinct foams (Ni foam, Cu coated Ni foam, and Cu–Ni alloy foam), and Cu joints linked to these composite solders.The skeleton of the Cu–Ni alloy foam (Fig. 8a–c) exhibited a rough surface morphology indicating the ability of this foam type to optimally promote molten Sn solder infiltration since substrates with high surface roughness promote solder wettability easily. The cross-sectional images (Fig. 8d–f) of the composite solder foils showed the absence of a reaction layer on the skeleton of the Cu coated Ni foam. Moreover, a gray contrasting IMC layer having approximately 2.5 μm was generated on the skeletal surface of the Cu–Ni alloy foam/Sn composite solder, indicating superior rate of reaction with the solder matrix than the other two foam types.

Tensile strength gains of 161.1%, 200.2%, and 234.4% for the Ni/Sn, Cu coated Ni/Sn, and Cu–Ni alloy/Sn composite solder, respectively, were noted when compared to the tensile strength of the plain Sn solder. The enhanced interfacial reaction between the reinforcing foam and the solder was highly critical in achieving adequate strengthening. Hence, the superior tensile strength demonstrated by the Cu–Ni alloy/Sn composite solder. The electron back scatter diffraction (EBSD) for the phase distribution of Cu joints with the different composite solders for 1 h demonstrated the $(Cu,Ni)_6Sn_5$ as the main phase in the solder seam with few Ni skeleton structures and residual Sn solder distributed in it. The remaining metal skeleton structures in the solder seam diminished slowly in the three joint types leading to significant rise in the rate of dissolution of the metal skeletons.

The mean grain sizes of the $(Cu,Ni)_6Sn_5$ phase and Sn matrix present in the solder joints prepared with Ni/Sn, Cu coated Ni/Sn, and Cu–Ni alloy/Sn were 6.8 m, 6.3 m, and 4.8 m, respectively, according to the EBSD grain mapping pictures (Fig. 8g–i). The grains at the center of the solder seam of the joints prepared with Cu coated Ni and Cu–Ni alloy composite solders were highly refined but grew larger close to the Cu substrates in comparison to the homogeneous grains present in the joint prepared with Ni/Sn composite solder. Meanwhile, the joints prepared (at 260 °C for 60 min) using Cu–Ni alloy/Sn composite solder demonstrated the superior shear strength (61.2 MPa), whereas those prepared with Ni foam exhibited the lowest (52.7 MPa). According to the results of the fractography investigation, all solder joints had cracks that primarily came from the solder seam. More specifically, the Cu–Ni alloy/Sn composite solders created substantial amounts of $(Cu,Ni)_6Sn_5$ particles, which had the smallest grain sizes in the joints they formed. Hence, the superior strength of the joints prepared with the Cu–Ni alloy/Sn composite solders.

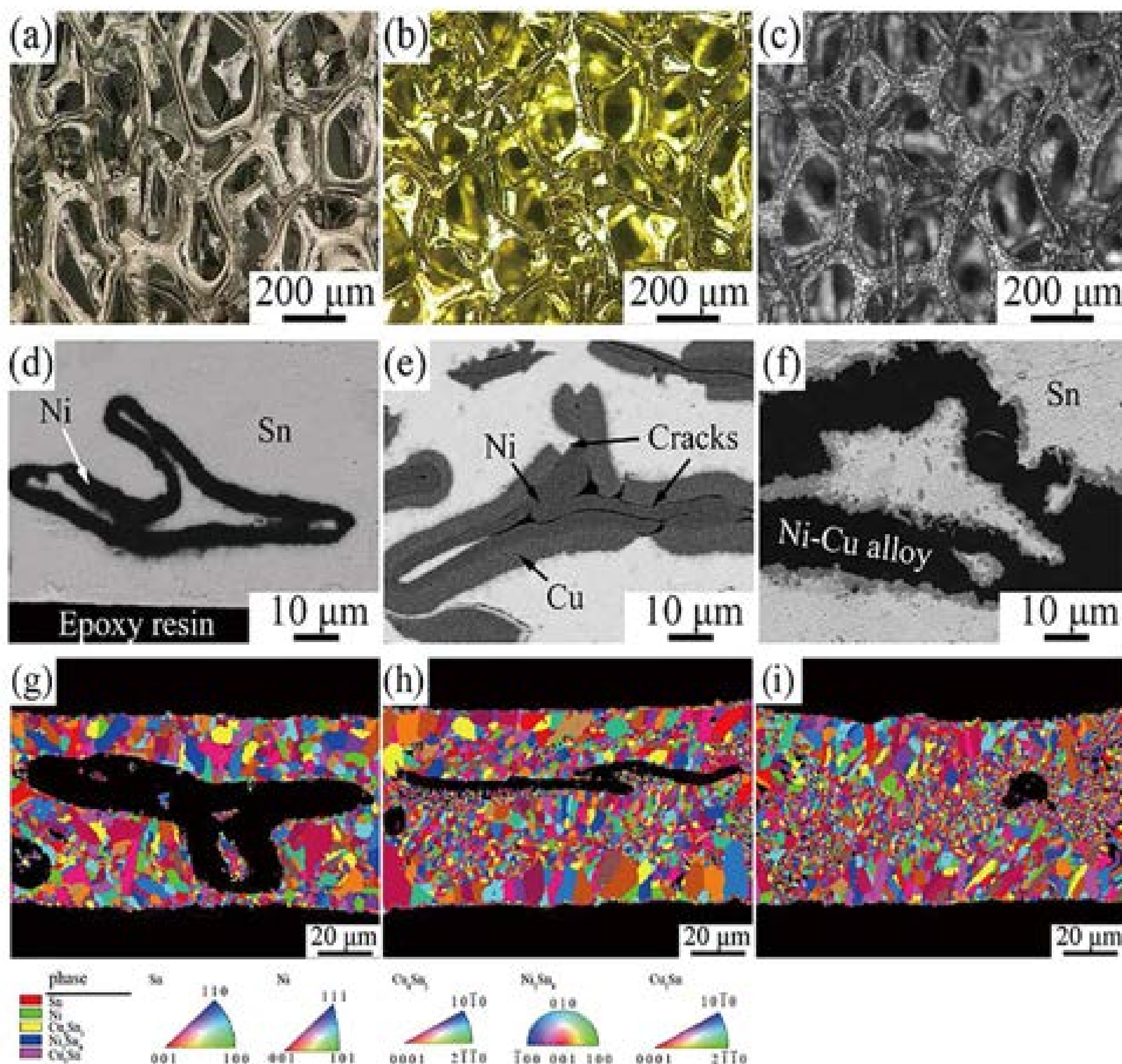

Fig. 8 – Microstructures of (a) Ni foam, (b) Cu coated Ni foam, (c) Cu–Ni alloy foam; cross-section of Sn-based composite solders reinforced with (d) Ni foam, (e) Cu coated Ni foam, (f) Cu–Ni alloy foam; EBSD images of grain mapping of Cu joints soldered for 60 min utilizing (g) Ni foam, (h) Cu coated Ni foam, (i) Cu–Ni alloy foam [96].

The same set of authors worked on a complementing study focusing on the characterization of isothermal diffusion reaction-induced microstructure of Cu interconnects bonded with Ni-foam reinforced Sn-based composite solder [97]. The metallurgical reaction of the solder seam subjected to prolonged soldering duration was reported to be controlled by the solid-state diffusion process, during which Ni segregated at the $Cu_3Sn/(Cu,Ni)_6Sn_5$ interface and inhibited Cu diffusion from the Cu board into the solder seam. This suggests that Cu supply into the solder seam can be inhibited, whilst Ni can maintain its diffusion into the solder seam through the progressing Ni–Sn reaction. More so, grain boundary diffusion of Cu and Sn was identified as the primary controlling mechanism for the growth rate of $(Ni,Cu)_3Sn_4$ phase. The $(Ni,Cu)_3Sn_4$ phase's average size decreased as a result of progressive nucleation of new grains, which outpaced grain expansion. Meanwhile, because of the high nucleation rate, the $(Ni,Cu)_3Sn_4$ grains that surrounded the Ni skeleton's surface exhibited highly refined grain sizes.In order to produce highly reliable joints, it is worth noting that high purity of Ni-foam must be ensured prior to its addition as a component for soldering operation. In line with this, Wang et al. [98] utilized 5% hydrochloric acid and ethanol to ensure the removal of oxide impurities before dipping into molten Sn solder for the ultrasonic-aided soldering of Cu alloy. According to the comparative study on the effect of ultrasonic-aided soldering duration on the shear strength of Cu/Ni–Sn/Cu joints, the following findings were observed: (i) shear strength of 24 MPa was measured at 5 s with fracture occurring within the solder, (ii) shear strength of 58 MPa was measured at 20 s with

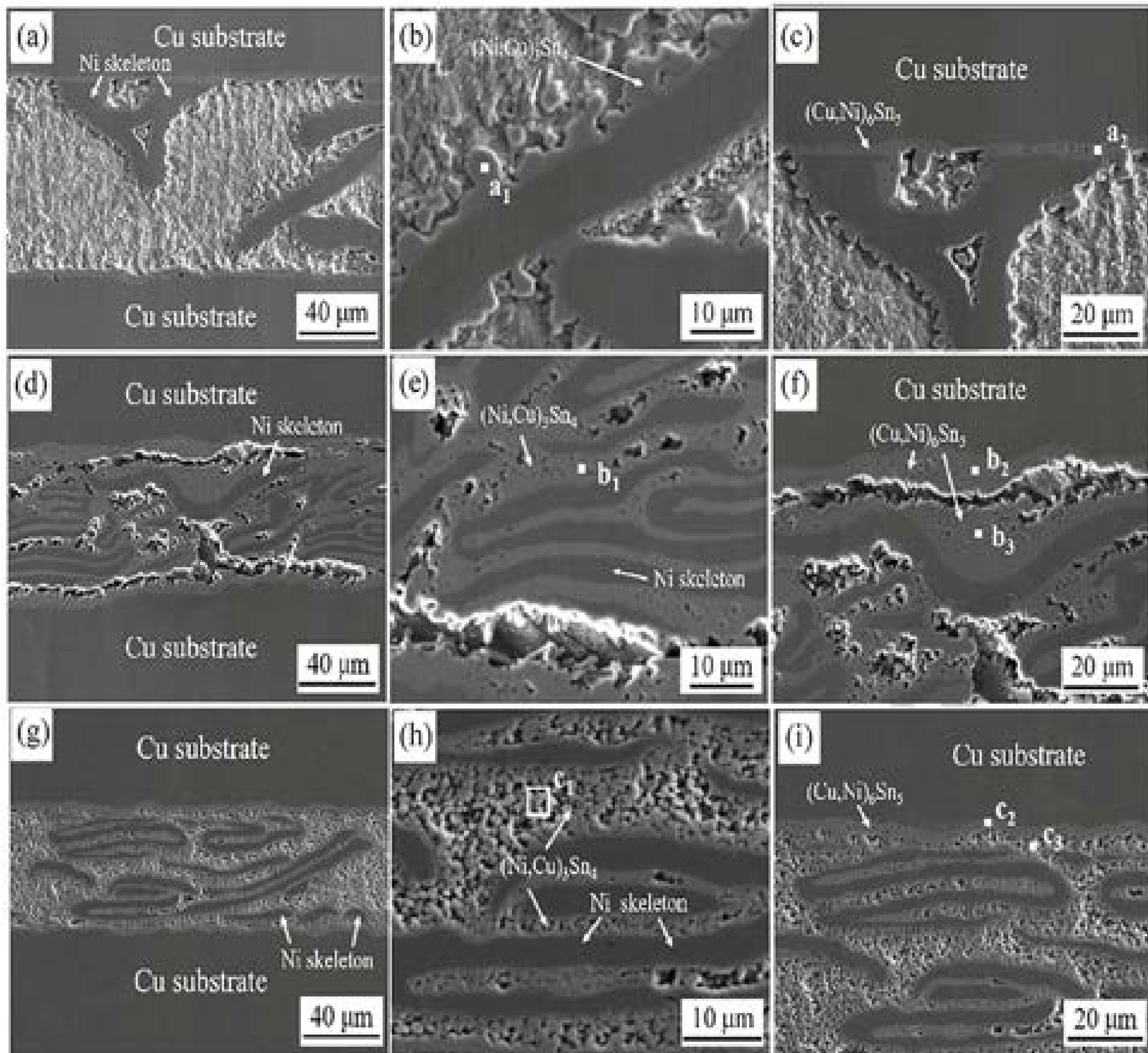

Fig. 9 – Microstructures of (a) cross-section, (b) Ni foam interlayer, (c) soldering seam/Cu interface for Cu/Ni–Sn/Cu at 250 °C for 5 s; microstructures of (d) cross-section, (e) Ni foam interlayer, (f) soldering seam/Cu interface for Cu/Ni–Sn/Cu at 250 °C for 20 s; microstructures of (g) cross-section, (h) Ni foam interlayer, (i) soldering seam/Cu interface for Cu/Ni–Sn/Cu at 250 °C for 30 s [99].

fracture occurring along the Ni-foam within the solder, and (iii) highest shear strength of 64 MPa was measured at 30 s with fracture occurring within the solder close to the reaction interface.

Inspired by the capacity for the production of durable joints at reduced temperature within a limited bonding period, Xiao et al. [99] successfully utilized ultrasonic vibration to solder copper with Ni foam-reinforced Sn composite solder. The microstructures of the Cu/Ni–Sn/Cu joint (Fig. 9a–c) subjected to ultrasonic soldering at 250 °C for 5 s reveal random distribution of Ni skeletons in the Sn-based solder and seamless layers of reaction on both the Cu substrates and Ni skeletons. The EDS of the region marked a_1 revealed that the $(Ni,Cu)_3Sn_4$ phase developed on the Ni skeletal surface while that of the region a_2 revealed the $(Cu,Ni)_6Sn_5$ phase mainly formed on the Cu substrate. According to the microstructures of the Cu/Ni–Sn/Cu joint that was ultrasonically soldered for 20 s (Fig. 9e and f), the amount of Sn and the thickness of the Ni skeleton abruptly decrease in comparison to the joint soldered for 5 s. Similar phases/location as those of the joint soldered for 5 s were detected in the joint soldered for 20 s except for the Cu_3Sn located on the Cu substrate as well as the combination of $(Cu,Ni)_6Sn_5$ and $(Ni,Cu)_3Sn_4$ phases present on the Ni skeleton surface close to the Cu substrate.

Meanwhile, a significant change in morphology (Fig. 9g–i) was observed in the solder joint prepared for 30 s as compared with the 20 s counterpart. The thin layer of Cu_3Sn has been completely consumed with the formation of micro-sized black

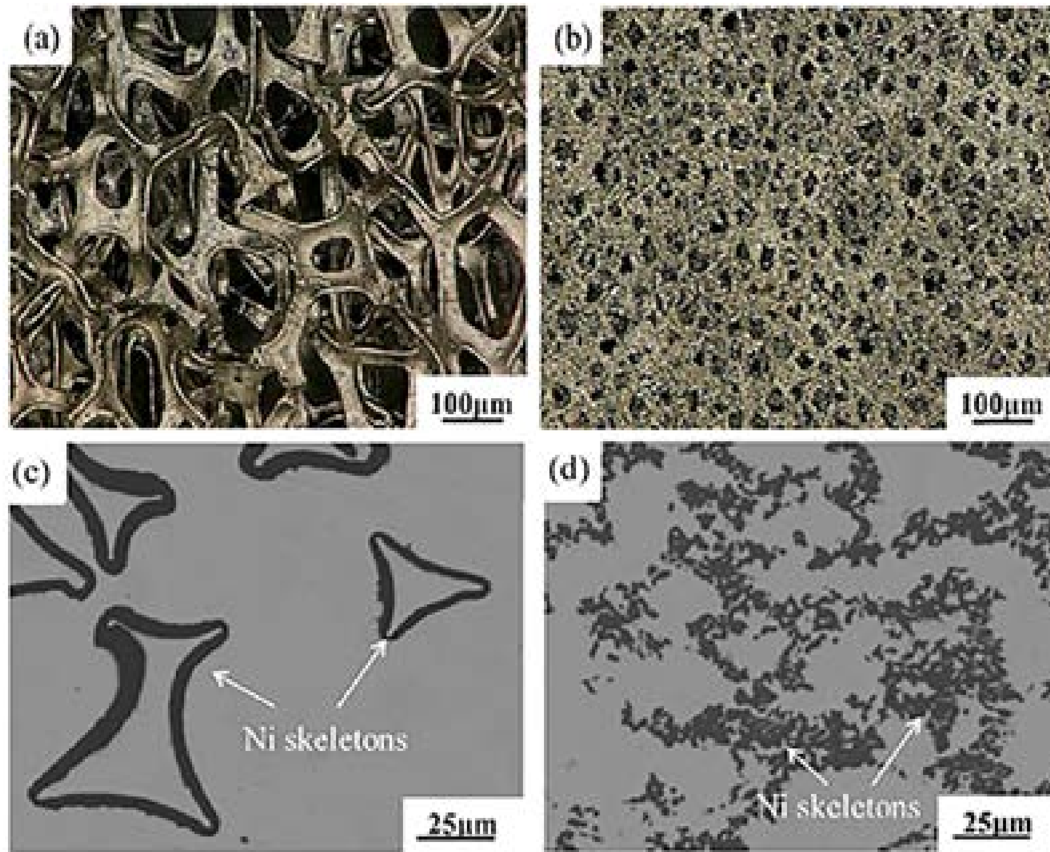

Fig. 10 – Images of Ni foams with (a) 80%, and (b) 60% porosities; cross-section of (c) Ni80–Sn, and (d) Ni60–Sn foils [101].

particles (predominantly composed of $(Ni,Cu)_3Sn_4$ phase), which dispersed uniformly in the solder seam with few Ni skeleton structures dispersed at random among them. Additionally, the uniformly dispersed micro-sized $(Ni,Cu)_3Sn_4$ particles in the solder seam demonstrated potential as reinforcing areas in the solder with the ability to increase the joint strength. The effect of microstructural evolution was observed in the shear test conducted on the Cu/Ni–Sn/Cu ultrasonically soldered for 30 s, which exhibited the superior strength of 64.9 MPa while 52.5 MPa and 26.4 MPa were measured for the joints soldered for 20 s and 5 s, respectively. The homogenously dispersed micro-sized $(Ni,Cu)_3Sn_4$ particles in the solder seam were suggested to be responsible for the strengthening of the joint based on the Orowan strengthening mechanism.

In another study by the same team [100], the microstructure and strength integrity of 075-Al alloy joints soldered using an ultrasonic process with Ni-foam/Sn composite solder were investigated. It was discovered that the Sn-based solder completely filled the pores in the Ni-foam, proving that the Ni skeleton and Sn solder had a strong link, thanks to the formation of Ni_3Sn_4 on the surface of the Ni skeleton. At the Al substrates and with increased ultrasonic soldering, the Al_3Ni IMC layer was created. Al atoms from the Al substrates diffused through the solder to precipitate the evolution of Al_3Ni phase on the Ni skeleton structure in addition to the existing Ni_3Sn_4 phase. The wetting between the Ni-foam/Sn composite solder layer and the Al substrate was therefore determined to be caused by the mechanical friction impact of the long duration (over 10 s) ultrasonic soldering. It was also deduced from the shear strength measurement that the strip type Ni skeleton of the Ni-foam alongside the Al_3Ni and Ni_3Sn_4 IMCs played a critical role in strengthening the Al/Ni–Sn/Al joint.

A similar soldering process was employed in bonding 2024 Al alloy for use in the aerospace and automotive industries [101]. Two types of Ni-foam were used in the study including; (i) Ni-foam having 80% porosity, 150 μm mean pore diameter and with continuous, interweaved and intertwined Ni skeletons (Fig. 10a), and (ii) Ni-foam with 60% porosity, 50 μm mean pore diameter and Ni skeletons with struts that are continuous but more compact (Fig. 10b). From the cross-section micrographs, triangular hollow pores are present in the Ni80–Sn struts (Fig. 10c), while that of the Ni60–Sn are approximately solid (Fig. 10d). The Ni foam maintained 3D seamless network architecture and Sn solder dispersed in the cells of the Ni foam which accounts for the interpenetrating strengthening structure of the Ni-foam/Sn composite solder.

With the introduction of Ni foams with 60% and 80% porosities, the tensile strength of the composite solders increased by 219.3% and 344.8%, respectively. Moreover, the Ni skeletons of Al/Ni80–Sn/Al joint maintained a 3D seamless network architecture and demonstrated a striped distribution pattern. However, portions of the Ni skeletons for the Al/Ni60–Sn/Al joint were damaged and lost their seamless structure as the ultrasonic bonding duration increased. The shear strength data supported the impact of the

Table 2 – The effect of Ni foam on the solder reliability of lead-free solder joints.

Solder material	Solder reliability improvement	Ref.
Sn–58Bi	The brittle interfacial fracture common to joints prepared with SnBi solder was restrained by the incorporation of porous Ni.	[85]
Sn-based	The skeleton of the Ni foam actuated the progressive nucleation of new $(Ni,Cu)_3Sn_4$ grains and resulted in their average grain size reduction.	[97]
Sn-based	Treating the Ni foam with 5% HCl and ethanol solution enhanced the shear strength of the Sn solder joint.	[98]
Sn-based	The homogenous dispersion of the $(Ni,Cu)_3Sn_4$ particles in the solder seam which was actuated by the Ni skeleton close to the Cu substrate enhanced the joint strength based on the Orowan strengthening mechanism.	[99]
Sn-based	Ultrasonic soldering aided the wetting between Ni foam/Sn solder and the Al substrate, thereby improving the capacity of the Ni skeleton alongside the formed Al_3Ni and Ni_3Sn_4 IMCs in strengthening the developed joint.	[100,101]
Sn-based	Dissociation of the IMCs into uniformly dispersed refined particles accompanied by Ni skeletons inhibited fracture propagation and enhanced the joint strength.	[102]
Sn-3.5Ag	The deposition of Cr layer on 500 nm thick Ni interlayer contributed immensely in improving the strength reliability of reactively bonded solder joints.	[103]

aforementioned discovery because they showed that, for comparable bonding conditions, the Al/Ni80–Sn/Al joint outperformed its Al/Ni60–Sn/Al counterpart.

With the utilization of ultrasonic-assisted soldering, the introduction of Ni foam as a reinforcing phase in Sn-based solder intensified the metallurgical reactivity owing to substantial quantity of liquid/solid interface, and refined IMC grains by ultrasonic cavitation [102]. Moreover, the dissolution of Ni skeletons occurred as ultrasonic time increased and resulted in the peeling off of the IMCs from the substrates and their subsequent disintegration into smaller particles. Thereafter, the IMCs dissociated slowly into refined grains and dispersed uniformly in the entire solder seam under the influence of cavitation. The uniformly dispersed IMC granules and Ni skeleton structures inhibited fracture propagation and enhanced the strength of the joints formed on the Cu substrates.

Namazu et al. investigated the joint effects of exothermic reactive layer (Al/Ni) and metal interlayer on the fracture patterns of solid single crystal silicon (SCS) with reactively attached Sn-3.5Ag solder joint using two types of interlayer components (500 nm thick Ni single interlayer and 500 nm thick Ni with 50 nm Cr double layer) [103]. For the double interlayer, it was observed that the Cr layer deposit between the Ni layer and SCS promoted the strengthening of the solder interconnects prepared using the Al/Ni reactive bonding. Thus, it was revealed that increasing the thickness of the Al/Ni and adding a layer of Cr between the Ni layer and the SCS are essential for enhanced mechanical strength and reliability of reactively bonded solder joints. According to the fractography, the development of a silicide layer at the Ni single interlayer-SCS interface reduced the adhesion strength between Ni and SCS in comparison to the adhesion strengths of reacted NiAl, SnAg, and NiAl–SnAg. However, the presence of Cr in the double interlayer at the Ni and SCS enhanced the bond strength between SnAg and SCS owing to better affinity between Cr and SCS.

The comparative study between two solder joints prepared with different types of porous Ni (i.e. 110 PPI and 500 PPI) showed that the SnBi@500P–Ni demonstrated more porous Ni skeletons and barely few solder parts were retained in the solder bulk [85]. This finding shows that the SnBi@500P–Ni is capable of operating at high temperatures while still being suitable for low-temperature soldering. The shear strength of joint reinforced with the 110 PPI demonstrated the highest strength relative to others. According to the fracture analysis conducted, the incorporation of porous Ni in the solder joints affected the crack propagation paths in the solder joints. Thereby, indicating the capacity of the porous Ni in limiting the brittle interfacial fracture common in SnBi solder joint.

A summary of the solder joint reliability improvement by Ni foam interlayer is presented in Table 2. This interlayer material demonstrated capacity to revamp existing lead-free solders in meeting the conditions of low-temperature soldering and high-temperature service operation. More so, the applicability of the Ni foam-reinforced composite solders on different substrates including Al substrates demonstrates an immense potential of the Ni-foam interlayer in improving solder joint reliability.

3.3. *Other interlayer materials*

Because graphene possesses a number of outstanding properties, including high electrical conductivity and excellent mechanical properties, it can be used to reinforce conventional solder alloys, which has been demonstrated in various studies [33,104]. Additionally, with optimum GNS reinforcement, it is possible to increase the electrical conductivity of solders by preventing electron scattering even in the presence of lattice defects [105–107]. The use of graphene as an interlayer in lead-free soldering process has shown remarkable IMC growth inhibition at the solder/substrate interface owing to its ability to protect the Cu substrate from oxidation and diffusion [108]. The study of Yang et al. [109] supports the

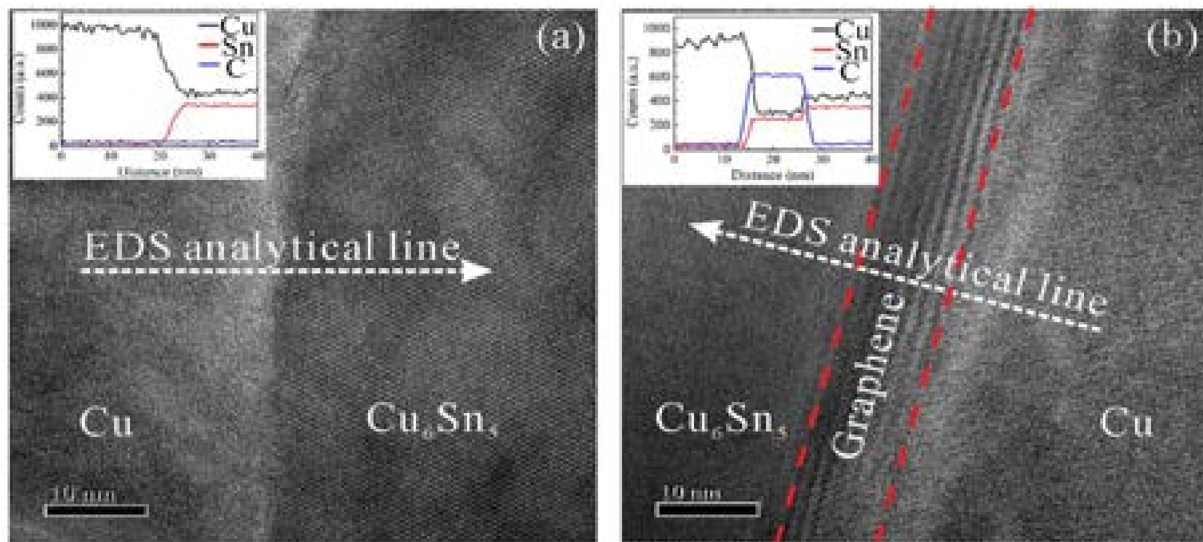

Fig. 11 – TEM micrographs showing the interface between Cu and Cu_6Sn_5 (a) without graphene interlayer and (b) with the graphene interlayer [109].

promising potentials of graphene interlayer in solder joints because, in contrast to the Sn–Cu counterpart, no appreciable IMC layer formation was seen at the bonding interface before and after 24 h of aging (150 °C). Moreover, the IMC layer thickness recorded for the Sn–Cu bonding interface after 72 h of aging was 2.63 μm whereas, that of the Sn-graphene-Cu counterpart was 1.14 μm. More so, the EDS analytical line of the TEM microstructure examined at the solder joint interface with graphene interlayer confirms the presence of C element layer (10 nm thickness) between the Cu and Cu_6Sn_5 and its inhibitory role in limiting Cu atoms diffusion from the Cu substrate (Fig. 11). It is also important to note that the Sn-graphene-Cu counterpart showed a lower rate of degradation of the shear strength values over time than the Sn–Cu counterpart.

The effect of the layer by layer graphene transfer at the interface between SAC305 solder and Cu pad on the interfacial reactions and IMC evolution control was investigated by Ko et al. [110]. A sandwich-like sample having Cu/3 layers of graphene/SAC305 solder/3 layers of graphene/Cu prepared after 10 times of reflow soldering (Fig. 12a) was employed to substantiate that the transferred graphene stayed unimpaired at the interfacial area after multiple reflow soldering. Upon analyzing the mechanically delaminated sample with the Raman spectroscopy (Fig. 12b) using the spots marked with red circle, the 2D and G peaks of graphene were detected in spite of 10 iterations of the reflow soldering. Whereas, in the blue marked region within the solder bulk, graphene peaks were not detected, confirming that the transferred graphene layers existed at the interface, in spite of several reflow processes.

After 10 iterations of the reflow soldering, the increasing height of the interfacial IMC with several graphene layers declined in excess of 20% relative to the interface of the plain Cu without graphene (Fig. 12c). For the Cu pad with no graphene (Fig. 12d), Cu atoms easily diffused and reacted with the Sn atoms in the liquid solder or the IMCs in the course of the reflow soldering. While in the case of the interface with graphene layers (Fig. 12e), Cu atoms passed through the honeycomb lattice of graphene to permeate and activate reaction with Sn in the solder. Hence, the Cu atoms were readily confined in the graphene lattice or lattice defects like vacancies which then resulted in increasing the diffusion path of Cu atoms. Moreover, the joint with graphene layer demonstrated superior shear strength relative to the joint without graphene, since the brittle fracture at the IMC region (Cu_6Sn_5/Cu_3Sn interface) was hindered by the inhibited IMC increment with graphene.

Despite its contribution in inhibiting the immoderate growth of IMCs according to Yang et al. [109], the chemical vapor deposition technique for the preparation of graphene on Cu foil and the subsequent transfer for bonding as interlayer between the Cu pad and solder are complex and easy to produce contaminants which are unsuitable for wide-ranging industrial production. In view of this, Yin et al. [111] prepared reduced graphene oxide (rGO) layer right on the Cu pad surface using the secondary reduction (SR) method. The C=O peak (288.44 eV), C-O peak (286.84 eV), and C-C peak (284.77 eV) are the highest observable constituents in the C 1s spectrum of graphene oxide nanosheets after performing XPS experiments to analyze the composition of the C elements in detail (Fig. 13a). In contrast, the rGO film's C 1s spectrum after the SR process (Fig. 13b) showed significantly smaller C=O and C-O. The C-C peak developed into a substantially symmetrical peak while the entire width at half maxima (FWHM) of the triple peaks also reduced relative to the GO nanosheets. Thus, confirming the secondary reduction method as a viable technique in the production of good quality rGO film containing lesser intricate chemical reactions on the surface as compared with the GO nanosheets.

Then, the potential of the produced rGO film to restrain the heightened growth of the IMCs was investigated by utilizing it as an interlayer component between the Cu pad and the Sn-3.0Ag-0.5Cu (SAC305) solder. Relative to the Cu/SAC305, the

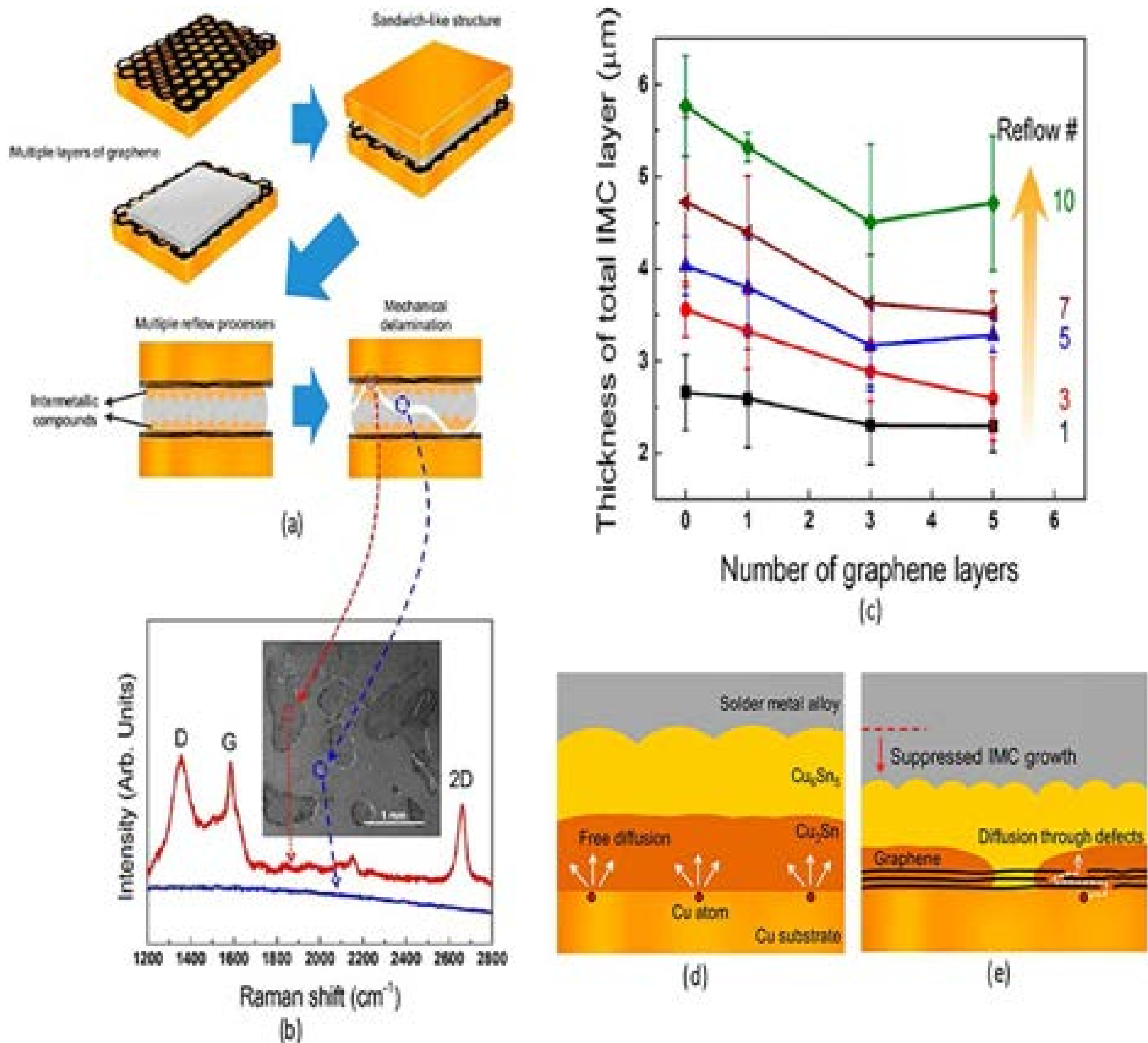

Fig. 12 – (a) Schematic showing the preparation of sandwich-like test specimen; (b) Raman spectra of delaminated interface after 10 iterations of the reflow soldering; (c) total IMC thickness versus number of graphene layers; schematic showing graphene influence on Cu diffusion for sample (d) without graphene layer, and (e) with several graphene layers [110].

interfacial IMC thickness for the aged (150 °C) Cu/rGO/SAC305 was inhibited beyond 30%, and the protruding region of IMC grains declined beyond 80%. Furthermore, the rGO interlayer had a lower rate of shear strength depreciation over time than the plain joint did. The incorporation of graphene/Cu nanocone array (NCA) composite on the plain Cu pad, according to Wang et al. [112], simultaneously addressed the high bonding temperature and aging deterioration problems that have been undermining the reliability of the Pb-free Cu bonding technology.

In order to overcome the roughness and numerous valleys present on the Cu NCA substrate, an ethylene-vinyl acetate (EVA)-aided graphene transfer approach was employed. The technique involves bringing the EVA/graphene batch into contact with the Cu NCA substrate in deionized water. Owing to the relatively high elastic modulus of the EVA (20 times larger relative to PMMA), a conformal coating on the Cu NCA was achieved and upon removing the EVA, a substantially better graphene coverage was obtained. While the bonding yield of aged Sn-graphene-Cu bonds prepared at 150 and 160 °C remained at 100%, that of the entire Sn–Cu bonds showed severe deterioration, regardless of the bonding temperature. This is measured as the ratio of solder joints with >20 MPa shear strength to the number of tested solder joints. The import from this is that graphene interlayer incorporation into the Sn–Cu bonds played remarkable function in inhibiting the impairment problem associated with the aging process.

The diffusion soldering process involves melting a low-melting metallic thin-film interlayer sandwiched between two high-melting substrates that have the ability to melt at low temperatures, in accordance with the basic principle of isothermal solidification [113]. The resultant IMCs formed exhibited higher melting temperature than the starting low-melting interlayer. Hence, its promising potential for low-

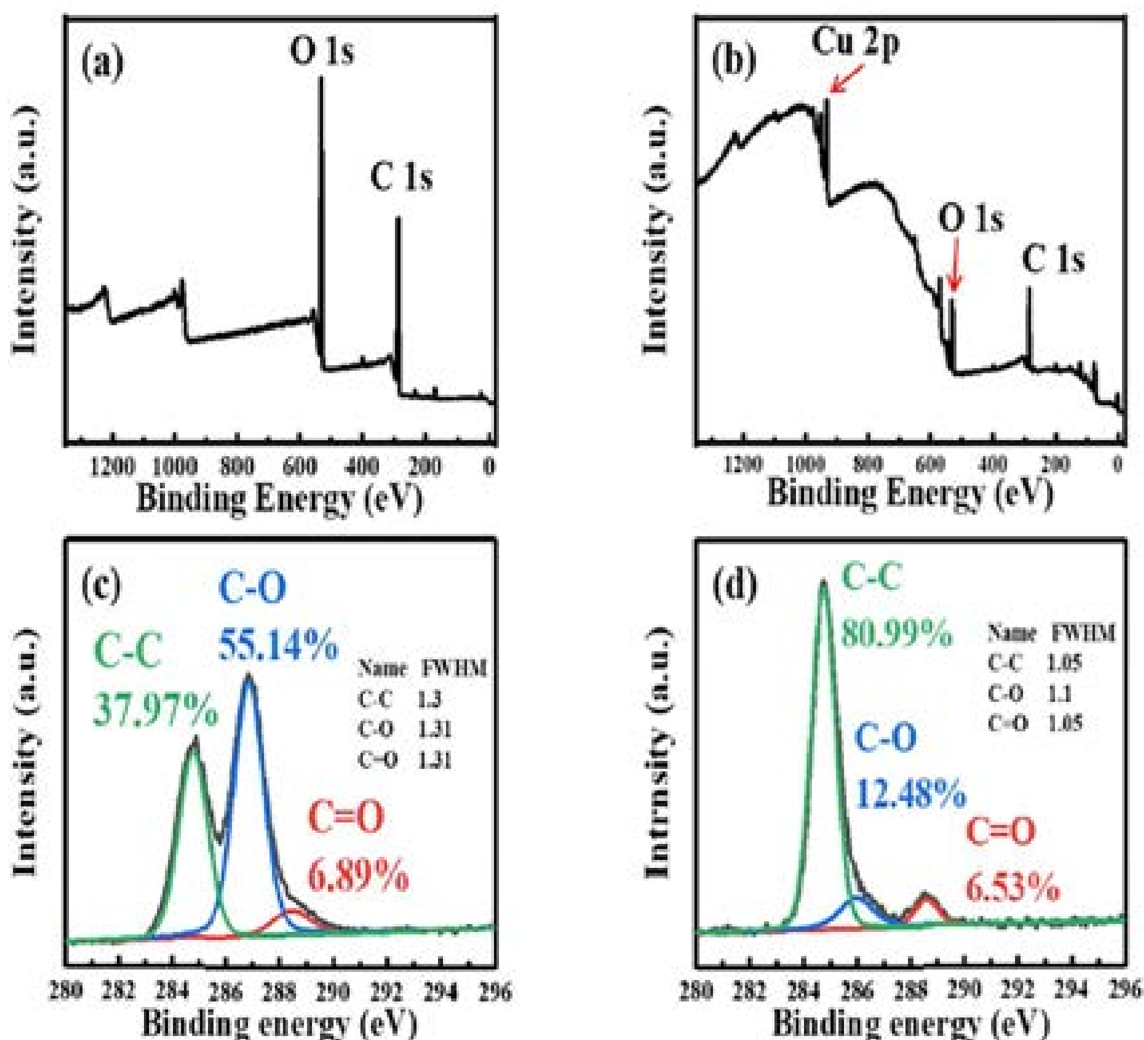

Fig. 13 – XPS spectra of (a) GO nanosheets, (b) rGO film with SR, and curve fit of (c) C 1s spectra for the GO nanosheets, (d) C 1s spectra for the rGO film with SR [111].

melting temperature bonding and utilization at higher operating temperature. On this note, the study of Liang et al. [114] on the incorporation of Sn interlayer for the diffusion soldering of Cu/Ti/Si and Au/Cu/Al_2O_3 at temperatures between 250 °C and 400 °C showed the elimination of the Sn interlayer during the process and formation of bilayer IMCs including: (i) $(Cu_{0.99}Au_{0.01})_6Sn_5$ corresponding to the η-Cu_6Sn_5 phase, and (ii) $(Au_{0.87}Cu_{0.13})Sn$ which corresponds to the δ-AuSn phase. Moreover, a desirable tensile strength of 132 kg/cm^2 corresponding to IMC thicknesses of 1.46 μm and 1.63 μm for the $(Au_{0.87}Cu_{0.13})Sn$ and $(Cu_{0.99}Au_{0.01})_6Sn_5$ IMC layers, respectively was achieved under diffusion soldering condition of 300 °C for 20 min.

The reinforcement of Sn-3.5Ag solder with Ag interlayer offered remarkable improvement in the derived joint [115]. In the two sandwich structures of Cu/Ag/Sn3.5Ag/Cu and Cu/Sn3.5Ag/Cu, the degree of asymmetrical growth of IMCs was higher in the latter than the former. By comparison, the thermomigration test revealed that the formation of Ag_3Sn layer at the upper interface owing to the presence of the Ag layer effectively suppressed the thermomigration-induced Cu flux. Meanwhile, the estimated $\int_{TM,Cu}$ which was approximately 0.3 times that without Ag_3Sn layer (Cu/Sn3.5Ag/Cu) further revealed that the Ag_3Sn has capacity to act as a barrier layer to inhibit the Cu flux. Furthermore, the crystallographic orientation of Sn was noticed to be influenced by Ag interlayer. The Cu/Ag/Sn3.5Ag/Cu joints demonstrated higher angle α relative to joints without Ag interlayer. This property further enhanced the effect of inhibition on $\int_{TM,Cu}$.

A summary of solder joint reliability improvement by other interlayer materials is presented in Table 3. Degradation issues associated with isothermal aging process was significantly inhibited by graphene interlayer in the solder joints. More so, some of these interlayer materials exhibited great potentials for low-melting temperature bonding and utilization at higher operating temperature.

4. ENImAg surface finish

As the demands for increased functionality of electronic gadgets increase coupled with their miniaturization, the

Table 3 – The effect of other interlayer materials on the solder reliability of lead-free solder joints.

Solder material	Solder reliability improvement	Ref.
Sn–Cu	Graphene interlayer addition was highly effective in suppressing IMC layer growth and deterioration rate of shear strength after aging.	[109]
SAC305	Impairment of graphene interlayer was prevented after multiple reflow soldering by utilizing the layer-by-layer technique which resulted in 20% decline in the interfacial IMC layer thickness.	[110]
SAC305	After isothermal aging, the solder reinforced with rGO interlayer demonstrated inhibited interfacial IMC thickness beyond 30%, decline in average projected area of IMC grains beyond 80% and inhibited shear strength deterioration.	[111]
Sn–Cu	The bonding yield of solders incorporated with graphene/Cu NCA interlayer remained at 100% despite the high bonding temperature and aging deterioration problems.	[112]
Sn-3.5Ag	The thermomigration-induced Cu flux was effectively suppressed by the introduction of an Ag interlayer.	[113]

expectations placed on the design and fabrication of the PCB have become greater. For some considerable time, the Electroless nickel immersion gold (ENIG) has been the prioritized, high-performance surface finish utilized in the printed circuit board (PCB) industry. Despite the clear benefits associated with this surface finish such as, superior solderability and corrosion resistance, the ENIG surface finish has its limitations [116]. They include; (i) high cost and price volatility of precious metal such as gold, (ii) the use of cyanide which is a strong chelator and a contaminant of wastewater stream, and (iii) the emergence of black line nickel solder joint defect (Fig. 14).

The recent choice of the electroless nickel immersion silver ENImAg surface finish has proven to be a highly effective and economically feasible alternative to the expensive ENIG. In addition, the use of the ENImAg prevents the additional cost incurred for the application and maintenance of the cyanide license required for the ENIG process. Herein, the performance of solder joints prepared using the ENImAg is comprehensively discussed. Fig. 15 presents the various steps involved in the preparation of the ENImAg surface finish [118]. Before investigating the nickel-doped SAC solder joint prepared using ENImAg substrate, Electroless Nickel (EN) was deposited at 90 °C for an hour on the pre-treated Cu substrate alongside chemical blends of sodium hypophosphite, sodium acetate, nickel sulfate and lead acetate [119]. Thereafter, the EN substrate was deposited in an ImAg solution at 40 °C for 8 min. The interfacial IMCs formed i.e. $(Cu,Ni)_6Sn_5$ and $(Ni,Cu)_3Sn_4$ exhibited different types of morphology and shape for each reflow stage which was attributed to multiple reflows and the type of surface finish utilized [120,121]. Moreover, the grain size of IMCs also increased with increasing reflow times.

By exploring the positive features of the ENImAg surface finish on the IMC layer evolution at the interface of the adjoining Sn–Ag solder, it was observed after multiple reflows that a thinner IMC layer (including NiSn–P) emerged for the solder joint prepared on the ENImAg as compared with that of bare Cu. Improved fracture strength with the use of the ENImAg surface finish was another significant finding that emerged from the study [122]. Elsewhere [123], the IMC thickness increased with increasing solder volume, however, the use of the ENImAg was able to mitigate the growth rate since the dissolution of Ni–P resulted in ultrafine grains. In the course of soldering using the ENImAg surface finish, the silver layer dissolves into the molten solder owing to dissolution of silver into the tin, thus exposing the nickel layer to interfacial reaction with the molten solder (see Fig. 16). It is worth noting that the Ag layer offers a protective solderable layer and ensures the solderability of the underlying

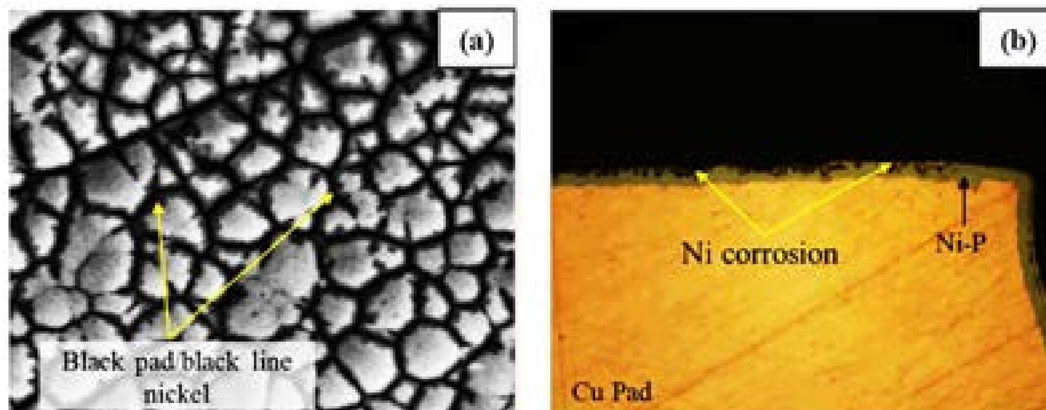

Fig. 14 – (a) Black pad between the nodules, and (b) Ni corrosion layer of ENIG surface finish [117].

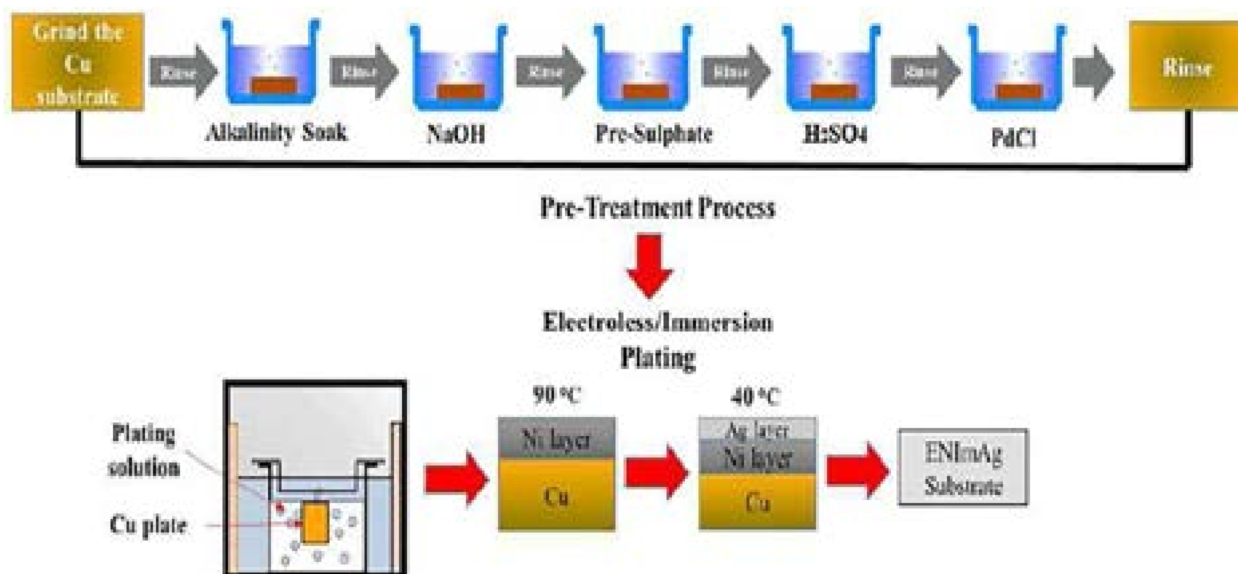

Fig. 15 – Schematic for the deposition process of electroless nickel immersion silver [118].

substrate. To ensure positive impact on solder joint, reduction in dissolution time and optimal solderability over different pad of printed circuit board, the thickness of the ImAg layer must be maintained at a value less than 1.0 μm [124–127].

Meanwhile, the thinner IMC layer demonstrated by SAC305/ENImAg solder joint triggered its enhanced shear strength relative to the solder joint prepared on bare Cu [128]. The finding was substantiated with the superior wetting performance of the SAC305/ENImAg which led to dispersion of more solder balls on the substrate and the creation of bigger joint area required to delay the initiation of crack propagation during the axial loading process. The same finding was presented in another complementing investigation where the ENImAg was used to prepare a solder joint having SAC405 as the base material [129].

Elsewhere [130], three kinds of IMC i.e. $(Cu,Ni)_6Sn_5$, $(Ni,Cu)_3Sn_4$ and $AgSn_3$ were observed at the interface between Sn-4.0Ag-0.5Cu solder and ENImAg surface finish exposed to different cooling rates and multiple reflow soldering. Only the $(Cu,Ni)_6Sn_5$ emerged after the first reflow while other IMCs evolved with increased reflow time. Hence, the increase in grain size and thickness of the IMC. More so, it was discovered that the IMC thickness and grain size increased rapidly with slower cooling rate (i.e. furnace cooling) compared to the faster cooling rate (i.e. water cooling). In addition to the interfacial IMC growth retardation prompted by the addition of bismuth reinforcement and the ENImAg surface finish, formation of spalling IMC emanating from high interfacial energies was detected at the Sn–Ag–Bi/ENImAg interface [131]. In the course of reflow soldering, internal stresses are induced between the thick compound layer and the substrate. Hence, the resultant effect of releasing the stress led to the formation of the spalling IMC. Elsewhere, the synergistic effect of utilizing CNTs/GNSs alongside the ENImAg surface finish was well marked in the barrier created for Sn and Cu atoms diffusion necessary for the formation of IMC and the

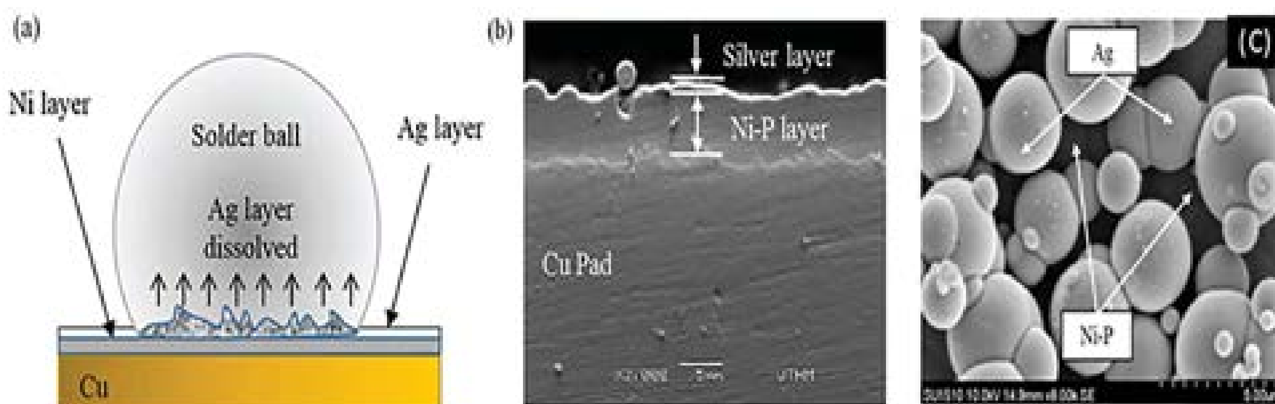

Fig. 16 – (a) Schematic of silver layer dissolution into molten solder at the interface, (b) SEM microstructure of the ENImAg/Cu substrate, and (c) Ag and Ni–P structures [123].

Table 4 – The effect of ENImAg surface finish on solder reliability of lead-free solder joints.

Solder material	Solder reliability improvement	Ref.
Sn–Ag	A thinner IMC layer and improved fracture strength were achieved with the use of the ENImAg surface finish.	[122]
Sn–Ag–Cu	The dissolution time of the Ni–P layer was significantly reduced which led to the growth inhibition of the IMC.	[123]
SAC305	The superior wetting performance triggered by the ENImAg surface finish resulted in the homogenous dispersion of more solder balls on the substrate and the emergence of a stronger joint area.	[128]
SAC405	The formation of a bigger joint area due to the superior wettability of the solder caused a delay in the initiation of crack propagation during axial loading process and shear strength improvement.	[129]
Sn–Ag–Bi	The Bi addition corroborated the ENImAg in retarding IMC growth and in raising the interfacial energies leading to the formation of spalling IMCs at the interface.	[131]
SAC105-CNTs/GNSs	The introduction of the carbon-based nanomaterials alongside the ENImAg slowed down the diffusion of the Sn and Cu atoms required for the formation of IMC.	[132,134]

effective strengthening of the composite solder joints formed with the Sn-1.0Ag-0.5Cu solder [132,133].

A summary of solder joint reliability improvement by utilizing the ENImAg surface is presented in Table 4. Clearly from the reviewed studies, the challenges associated with the use of other surface finishes, particularly, the ENIG have been significantly reduced by using the ENImAg surface finish. Besides the reduced cost of producing the ENImAg substrate demonstrated in these studies, the elimination of the black line nickel solder joint defect affirms the viability of ENImAg as a reliable candidate for the surface finish technology in soldering applications.

5. Geopolymer ceramics

The restriction on the use of lead in solder alloys in electronic packaging has piqued the interest of researchers in developing lead-free solder materials. Among the candidates for lead solder replacement, Sn–Ag–Cu (SAC) solder is a better choice, but it is not able to match the performance of lead solder in terms of wettability, joint strength and lower melting point [134,135]. However, incorporating reinforcing particles such as geopolymer ceramics into the matrix of a solder alloy has resulted in improved mechanical strength, reliability, and microstructure.

Mostapha et al. [136] investigated the effect of milling time and speed on the morphology and electrical properties of Sn-0.7Cu geopolymer ceramics separately reinforced with kaolin and fly ash. Fig. 17 shows that the composite solder reinforced with 1 wt% kaolin geopolymer ceramics (KGC) had the lowest resistivity (2.78 μΩcm) at 500 rpm milling speed and 10 h milling time. The low resistivity observed was attributed to the subangular structure and irregular shape of KGC. Elsewhere, the β-Sn dendrite in the bulk microstructure was significantly refined due to the addition of fly ash geopolymer ceramic to the SAC305 solder interconnect [137].

Zulkifli et al. [138] investigated the thickness of the IMC layer in a Sn-0.7Cu solder alloy reinforced with KGC and fly ash geopolymer. The IMC thickness was 2.0827 μm with 1.0 wt % fly ash geopolymer compared to 1.827 μm with the addition of 0.5 wt% KGC. Furthermore, by adding 1.5 wt% KGC and 0.5 wt% fly ash geopolymer, the melting temperatures of the reinforced solder were lowered to 228.83 °C and 228.15 °C, respectively. The presence of non-alloying particles with the ability to slightly alter the thermal properties of the host

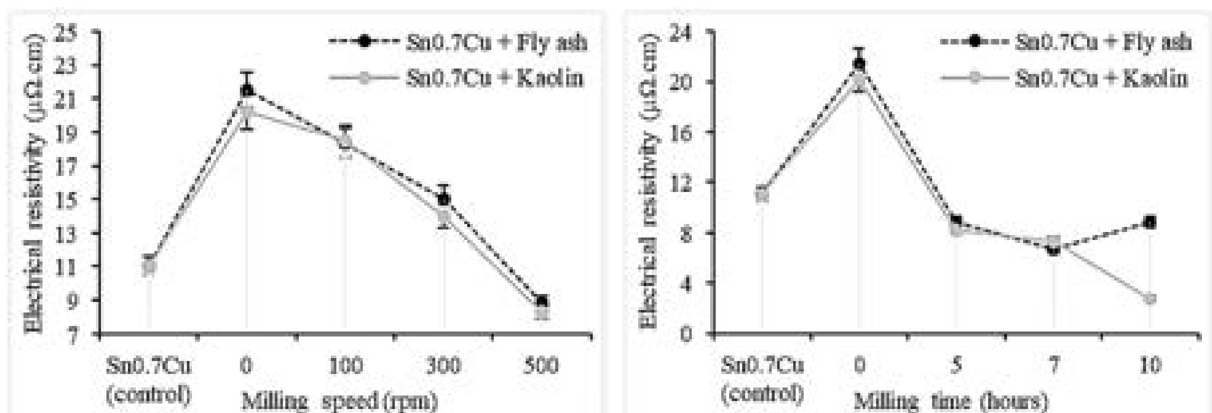

Fig. 17 – Effect on the electrical resistivity of Sn-0.7Cu composites solder with different (a) milling speed and (b) milling time [136].

solder system was attributed to the decrease in melting temperature. Because high melting temperature increases energy consumption, the inclusion of these reinforcing materials will consequently result in a significant decrease in the cost of thermal application during the reflow soldering process. The effect of 1.0 wt% KGC introduction on the wettability of the SAC305 solder was examined by Zaimi et al. [139]. The increased wettability with contact angle of 20.8° of the reinforced SAC305 composite solder was ascribed to the clustering of KGC particles at the interface of the liquid solder and flux, which caused surface tension. Zulkifli et al. [140] conducted a review of studies on the feasibility of fabricating geopolymer reinforced solder alloy. The assessment of chemical compositions, on the other hand, has been shown to have no negative effect on the solder joint performance.

Zaimi et al. [141] found that adding ceramic geopolymer improved the shear strength of SAC 305 solder significantly. The shear strength increased to 8.098 MPa with the addition of 0.5 wt% geopolymer, compared to 6.518 MPa for the plain solder. The enhanced shear strength of the composite solder was attributed to the geopolymer ceramis's refinement of the IMC morphology at the solder/substrate interface. Furthermore, when compared to monolithic SnCu having hardness of 6.48 HV, the influence of slag geopolymer on the SnCu solder increased hardness up to 7.84 HV [142]. In addition, the compressive strength of SnCu solder reinforced with slag geopolymer was significantly higher than that observed when kaolin and fly ash geopolymer were used. The improvement caused by the slag geopolymer was attributed to the homogeneous distribution of the slag particles along the grain boundaries of SnCu.

The same team [143] studied the influence of kaolin geopolymer ceramic on the microstructure and other properties of SAC305 solder. Outstanding performance was seen in the

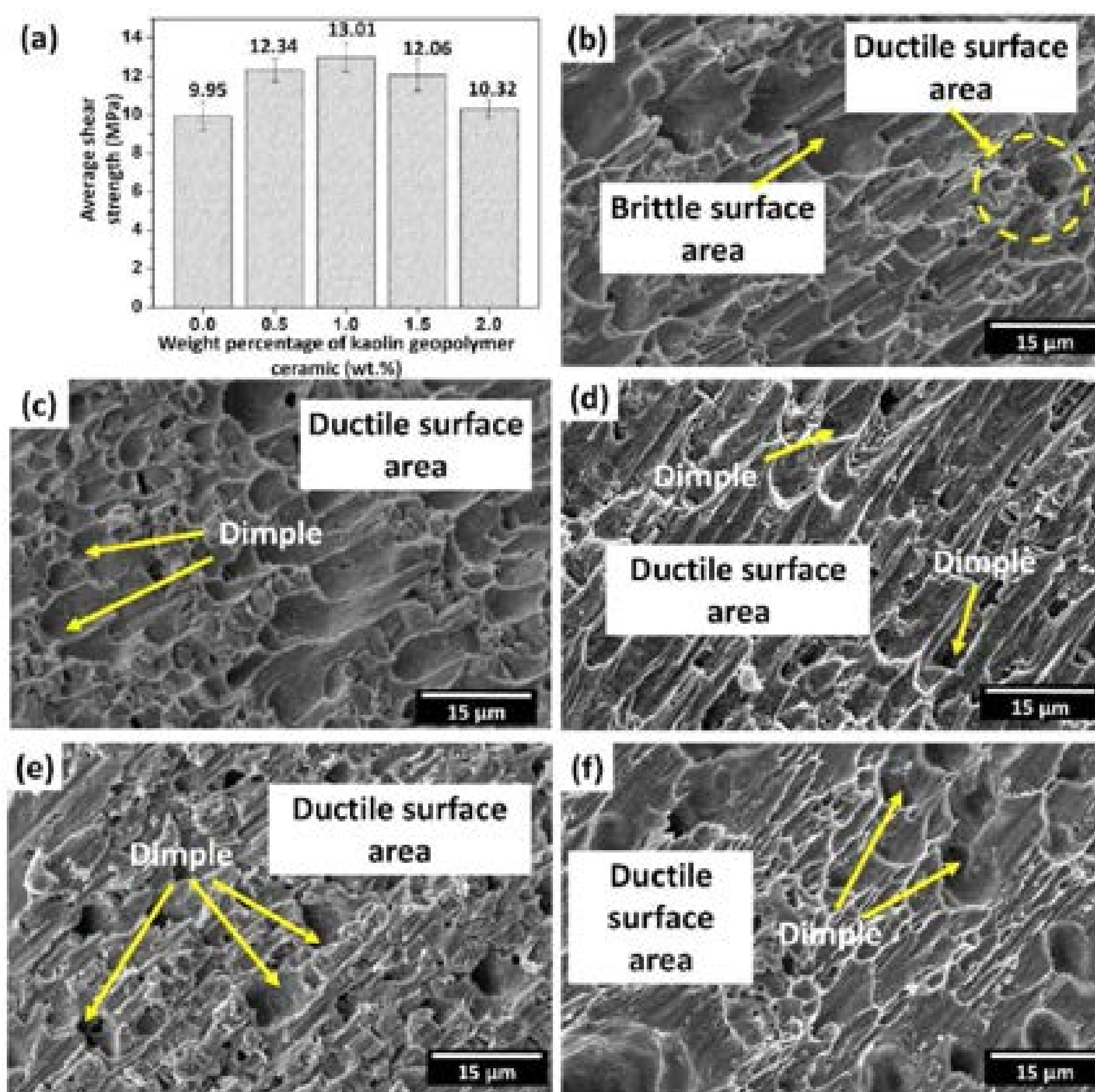

Fig. 18 – (a) Shear strength of SAC305 solder having various additions of KGC; FESEM micrographs of fracture surfaces of SAC305 composite solders doped with different KGC additions; (b) 0 wt %, (c) 0.5 wt%, (d) 1.0 wt%, (e) 1.5 wt%and (f) 2.0 wt% [143].

microstructure, thermal properties, spreadability, and joint strength of the composite solder reinforced with 1.0 wt% KGC. However, the addition of KGC aided in the refinement of the β-Sn phase while also limiting the growth of Cu_6Sn_5 and Ag_3Sn. In conclusion, the addition of KGC in various amounts significantly increased the shear strength of solder joints. As shown in Fig. 18, the shear strength increased to 13.01 MPa when 1.0 wt% KGC was added, compared to 9.95 MPa for pure lead-free solder. The authors attributed the excellent shear strength to the theory of dispersion strengthening.

The inhibition of the primary Cu_6Sn_5 and interfacial IMCs in the SAC solder joint doped with KGC led to 13% decline in shear strength after multiple reflow as compared to 27% shear strength decline demonstrated by the plain solder subjected to similar condition [144]. In another complementing study by similar authors [145], the KGC particles significantly suppressed the growth of Cu_3Sn IMC layer by 24% relative to the plain SAC305 solder during isothermal aging. The ability of the KGC particles to be adsorbed on the IMC surface, thereby inhibiting the diffusion of Cu at the interfacial IMC layer, was attributed to the suppression in the thickness of Cu_3Sn. The result was further supported by activation energy of 104 kJ/mol exhibited by the Cu_3Sn IMC of the SAC305-KGC and its lesser diffusion coefficient even at high temperature relative to the monolithic solder.

Table 5 summarizes the beneficial effects of the various geopolymer ceramics incorporated in Sn-based solder systems. Mechanical properties and microstructure improvements of reinforced lead-free solder have been highlighted.

6. Rotary magnetic field

By producing Lorentz forces, the rotational magnetic field can affect the flow and solidification behavior of liquid metal, which in turn affects the microstructure and performance [146–148]. Additionally, it works well to eliminate flaws, reduce nugget size, and enhance the solder joint's ability to dissipate plastic energy [149]. Comprehensive studies have been conducted to determine how best to use a rotational electromagnetic field to improve the drop reliability of Sn–Pb solders. These studies have confirmed that RMF can influence several aspects of solidification, such as decreasing dendritic or interlamellar spacing, changing heterogeneous columnar structures into homogeneous equiaxed structures, removing micro- and macro-segregation of solute constituents, improving IMC refinement and dispersion, and remarkably refining grain structure [150,151]. To determine the lowest creep rate of Sn–Bi solder solidified under RMF, the short term stress relaxation test (SRT) and strain relaxation and recovery test (SRRT) were performed [152]. Fig. 19 shows a schematic of the RMF experimental setup. A pair of 0.5 T permanent magnets with their N and S poles facing each other and rotating with a variable speed motor produced the magnetic field. The solidification process was performed by melting the Sn–20Bi solder alloy in a quartz tube at 600 °C for 1 h. Throughout the process, the molten alloy was continuously stirred in the revolving permanent magnets, and it was subsequently cooled at room temperature.

The samples with and without RMF clearly differ in terms of grain size and dendritic lamellar structure orientation. (Fig. 20a and b). A significant number of columnar dendrites in the β-Sn phase with alternate-layered lamella shape to a more rounded type were found in the microstructure of the Sn–20Bi solder without RMF. The fine eutectic regions intensified (see Fig. 20c and d) and exhibited a regular lamella structure having an alternate layer of Bi and Sn phases with little spacing. Additionally, the grain boundary region was evenly covered by these fine eutectic particles. Compared to the sample without RMF, the Sn–20Bi solder that had been hardened by RMF demonstrated greater resistance to stress and strain relaxation. Furthermore, the Sn–20Bi with and without RMF creep stress exponents of 9.8–8.1 and 9.5–6.3 (see Fig. 20e and f)

Table 5 – Summary of the influence of different geopolymer ceramics on the mechanical properties and microstructure of lead free solder composites.

Solder composite	Type of geopolymer	Solder reliability improvement	Ref.
Sn–0.7Cu	Kaolin and fly ash	With 1 wt% kaolin reinforcement, lowest resistivity of 2.78 μΩcm at 500 rpm milling speed and 10 h milling time was achieved.	[136]
Sn–0.7Cu	Kaolin and fly ash	**a.** 0.5 wt% of kaolin resulted in 1.827 μm as opposed to the 2.0827 μm observed with 1.0 wt% of fly ash. **b.** Melting temperature reduced to 228.83 °C with 1.5 wt% of kaolin and 228.15 °C with 0.5 wt% fly ash geopolymer.	[138]
Sn–3.0Ag–0.5Cu	Kaolin	The clustering of kaolin particles at the interface of the liquid solder and flux resulted in increased wettability with a contact angle of 20.8°.	[139]
Sn–3.0Ag–0.5Cu	Geopolymer ceramic	The addition of 0.5 wt% geopolymer enhanced shear strength up to 8.098 MPa as compared to 6.518 MPa for the plain solder.	[141]
SnCu	Slag, kaolin and fly ash	Improvements in hardness up to 7.84 HV and the compressive strength were observed to be greater for solder with slag reinforcement than when kaolin and fly ash were used.	[142]
Sn–3.0Ag–0.5Cu	Kaolin	**a.** The introduction of 1.0 wt% of kaolin led to excellent microstructure, thermal properties, spreadability and joint strength. **b.** Shear strength increased to 13.01 MPa with 1.0 wt% kaolin compared to the 9.95 MPa for pure solder.	[143]
Sn–3.0Ag–0.5Cu	Kaolin	The introduction of KGC led to activation energy of 104 kJ/mol and lesser diffusion coefficient of the Cu_3Sn IMC during isothermal aging.	[145]

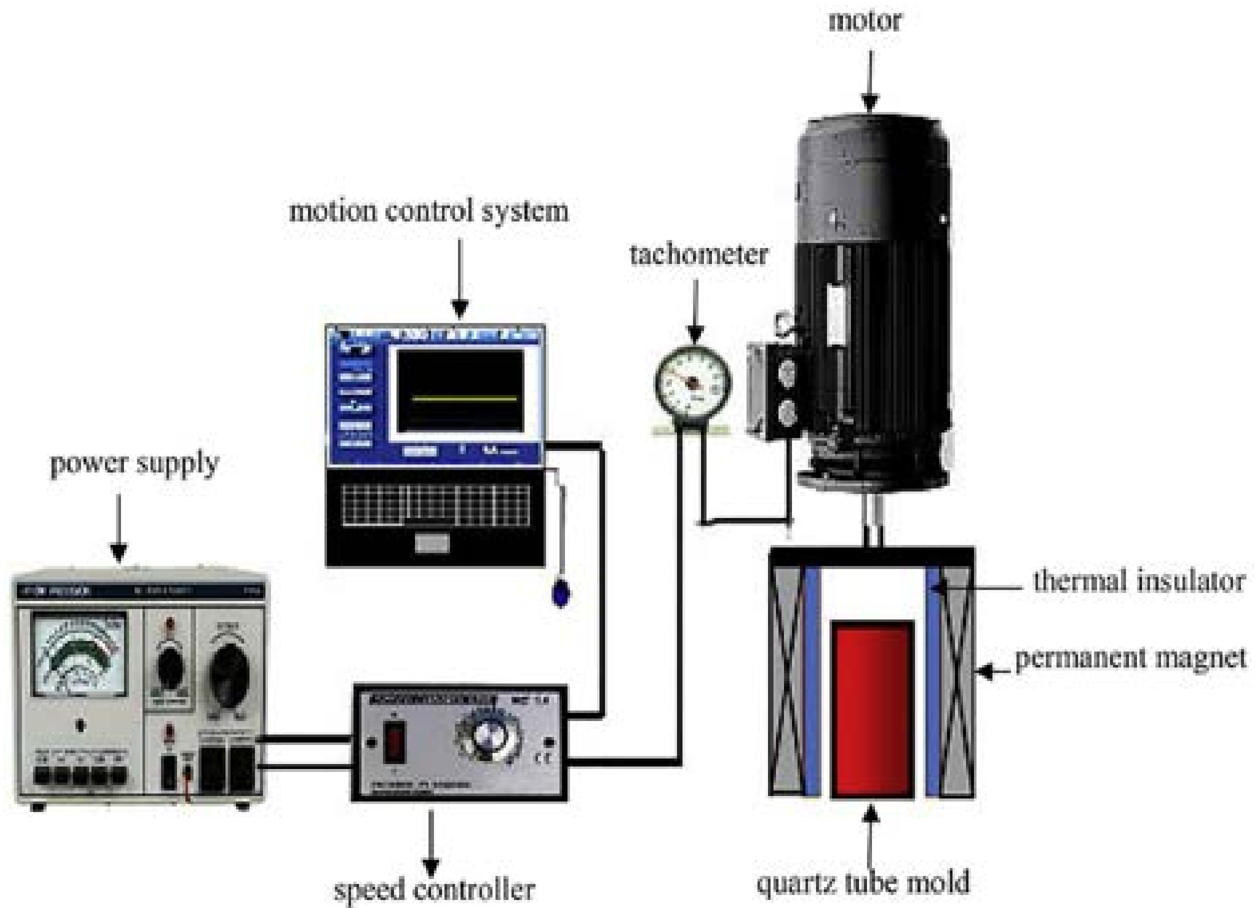

Fig. 19 – A schematic diagram of the RMF process [152].

indicate a sizable number of fine-grained lamella eutectic structures in Sn–20Bi solder.

Due to its capacity to enhance the reliability of lead-free solders, an assessment of the influence of RMF on solidification microstructure and tensile behavior of Sn–20Bi and Sn–20Bi-0.4Cu was performed [153]. Three critical non-dimensional parameters were taken into account to control the liquid melt that can yield the needed growing interface character and in turn meet the industrial requirements [147]: a) The Taylor number (T_a), which establishes the magnetic force by RMF; b) the Reynolds number (R_e), which measures the magnetic field skin depth in relation to cylinder radius; and c) the Hartmann number (H_a), which is essential for the assessment of field velocity resulting from the electromotive force and viscous force.

$$H_a = BR\sqrt{\frac{\sigma}{2\mu}} \quad (1)$$

$$R_e = \frac{\omega R^2}{\nu} \quad (2)$$

$$T_a = R_e \bullet H_a^2 = \frac{\sigma \omega B2R^4}{2\rho\nu 2} \quad (3)$$

where ω is the angular velocity, R is the cylinder radius (1.5 cm). The magnetic field is characterized by magnetic induction B, the viscosity by μ while ρ, ν and σ stand for the density, kinematic viscosity and electrical conductivity of the Sn matrix. The H_a and R_e measured for the Sn–20Bi solders were 248.1 and 1.3×10^5, respectively. Thus, the magnetic T_a of 7.9×10^9 was attained indicating the consideration of the melt flow as a turbulent flow [150,154] and the subsequent reduction in the quantity of unwanted dendrite components.

Due to the forced melt convection and the uniformity of the concentration and temperature fields triggered by RMF, the coarse-Sn dendrites, the eutectic structure, and Cu_6Sn_5 were effectively refined. In Sn–20Bi and Sn–20Bi-0.4Cu solders, the appearance of spheroidal or equiaxed grains suggests an activated columnar-to-equiaxed transition (CET) produced under the RMF state. With the application of RMF, the yield strength (YS) of Sn–20Bi solder was 14.2% higher than that without RMF, whereas ductility reduced slightly from 62% to 57%. The induction of CET and the appearance of a eutectic area in the structure created during the RMF state were attributed to the improvement in YS. As for the Sn–20Bi-0.4Cu, the increased ductility and lower strength were attributed to the RMF's substantial reduction in the amount of coarse Cu_6Sn_5 phase. El-Taher et al. reported on the effect of RMF on the physical properties of the Sn-0.5Ag-0.5Cu-2.0Sb-0.1Al (SAC0505SbAl) solder alloy [155]. Besides the transformation of the β-Sn grains from columnar to equiaxed, the RMF treatment remarkably decreased the aspect ratio of the β-

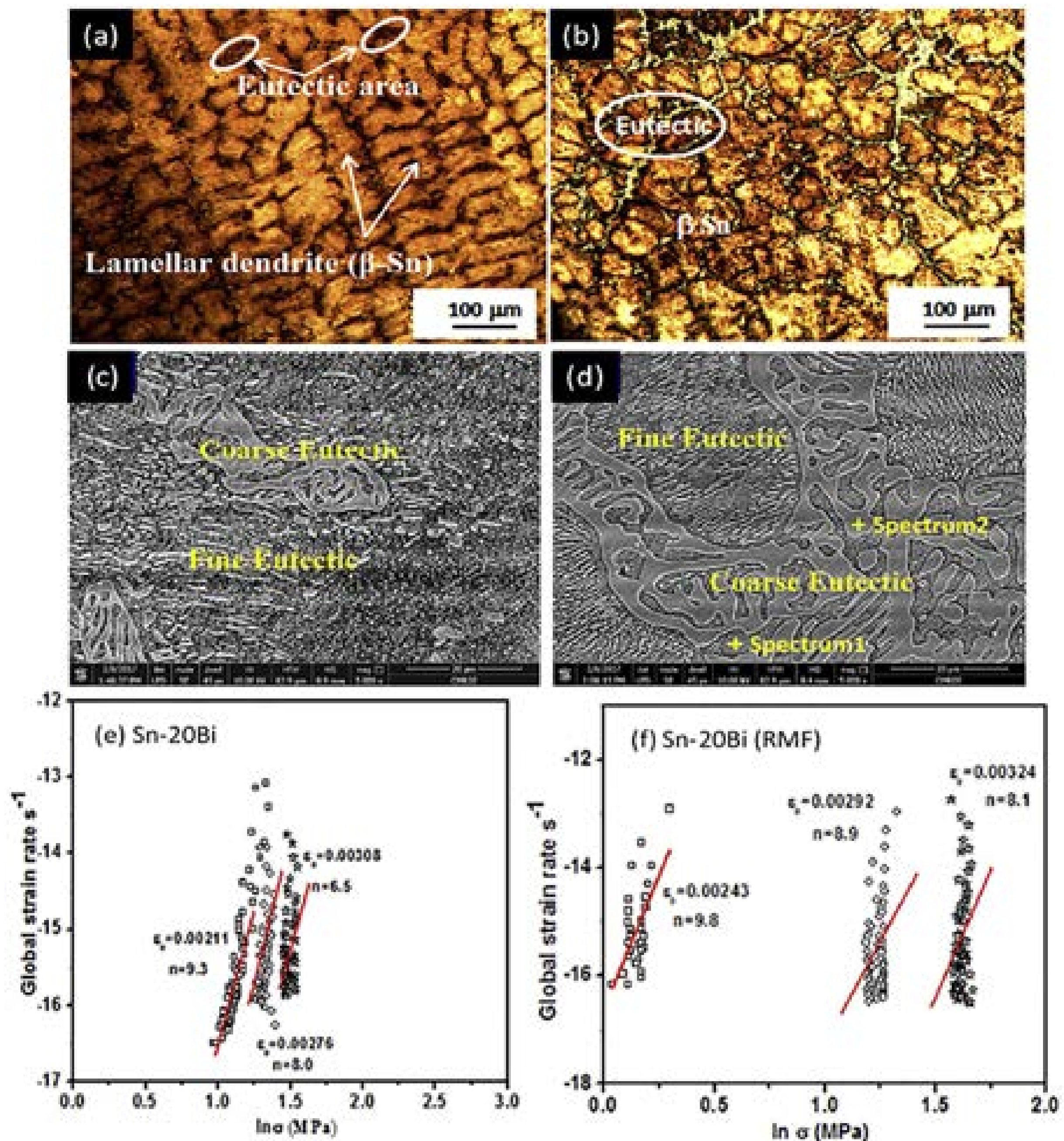

Fig. 20 – OM micrographs of (a) Sn–20Bi without RMF and (b) Sn–20Bi with RMF, FESEM micrographs of (c) Sn–20Bi without RMF and (d) Sn–20Bi with RMF, Stress dependence of global strain rate for Sn–20Bi solder (e) without RMF and (f) with RMF [152].

Sn grains. The IMCs detected by the XRD were SbSn, Cu_6Sn_5, AlCu and Ag_3Sn. Meanwhile, the extension of the RMF process duration until total sample solidification resulted in the evolution of thicker IMCs. For diffusion-assisted solid-state mechanism, the IMC evolution is dependent on the magnetic field intensity and diffusion coefficient. Therefore, the likelihood of jump in different magnetic routes and the diffusion coefficient were influenced by the variation in the magnetic properties of the principal elements (Al and Sn are paramagnetic, whereas Ag, Cu, and Sb are diamagnetic).

This substantiates the increased growth rate of the IMC with the application of RMF. Moreover, the combined effect of the equiaxed β-Sn grains and the coarse IMCs created due to RMF treatment led to the higher ductility and low Young's modulus exhibited by the Sn-0.5Ag-0.5Cu-2.0Sb-0.1Al solder. By implementing the RMF procedure, a slight drop in the melting point of the solder from 223.8 °C to 221.6 °C was observed which is essential for reducing surface tension and promoting quicker wetting of the solder alloy. The RMF also showed the ability to reduce undercooling from 13.1 °C to 9 °C

Table 6 – The effect of RMF on the solder reliability of lead-free solder joints.

Solder material	Solder reliability improvement	Ref.
Sn–20Bi	The uniform dispersion of fine eutectic particles across the grain boundaries promoted the superior resistance of the solder to stress and strain relaxation.	[152]
Sn–20Bi and Sn–20Bi-0.4Cu	The improvement in YS was ascribed to the induced CET and emergence of eutectic area in the structure developed under the RMF condition.	[153]
SAC0505SbAl	The implementation of RMF procedure led to decline in melting temperature while the combined effect of the equiaxed β-Sn grains and the coarse IMCs led to the higher ductility and low Young's modulus.	[155]
Sn-2.0Ag-2.0Zn	Increased creep resistance of 366% and superior creep rupture were achieved with the use of RMF.	[156]
Sn-2.0Ag-0.5Cu-2.0Zn	Mean grain sizes of the β-Sn and other IMCs reduced remarkably due to the microstructural refinement actuated by the RMF process.	[157]
SAC205	Substantial improvement of the tensile properties was achieved over the entire strain rate and temperature ranges.	[158]
Sn-1.0Ag-0.5Cu-0.5Sb-0.07Ce	A drop in the pasty range of the solder was achieved alongside 13.4% increase in elongation.	[159]

due to its influence on β-Sn grain refinement and nucleation. The findings are undoubtedly expected to provide a comprehensive insight into the performance of these newly discovered solder alloys under the influence of RMF that are potential candidates as Pb-free interconnects in microelectronic packaging industry.

The application of RMF to the Sn-2.0Ag-2.0Zn (SAZ) solder led to increased creep resistance of 366% and superior creep rupture time of 56.4% [156]. Their findings further showcase RMF as a reliable technique for enhancing the mechanical performance of Sn-based solder alloys for industrial applications. In another complementing study, the utilization of the RMF improved the microstructure and mechanical performance of Sn-2.0Ag-0.5Cu-2.0Zn (SACZ) solder [157]. Mean grain size of 10–20 μm for β-Sn as well as mean grain size of 5–10 μm for Cu_6Sn_5, Ag_3Sn and $(Cu,Ag)_5Zn_8$ were obtained for the SACZ solder prepared with RMF. The effect of the microstructural refinement was observed in the enhancement of the ultimate tensile strength, yield strength, elastic modulus and elongation by 110%, 112%, 119% and 108%, respectively. Similar findings were reported by the same team [158] for the SAC205 solder, where the tensile properties improved significantly with RMF application over the entire strain rate and temperature ranges.

Elsewhere [159], the Sn-1.0Ag-0.5Cu-0.5Sb-0.07Ce solder alloy was showcased as a plausible solution to the reliability issue of the Pb-free joint, thanks to the capacity of RMF processing in decreasing the pasty range of the solder from 5 to 4.7 °C as well as enhancing the mechanical properties (elongation increased by 13.4%). Meanwhile, the impact of RMF during the solidification process of Bi–Sn–Ag ternary eutectic alloy on the electrical resistivity revealed a rise from 35.6×10^{-5} to 38.6×10^{-5} Ω mm [160]. Furthermore, the electrical resistivity of the alloy increased from 35.4×10^{-5} to 43.5×10^{-5} Ω mm with rising temperature.

A summary of solder joint reliability enhancement by employing the RMF technology is presented in Table 6. Clearly from the reviewed studies, the utilization of the rotary magnetic field is beneficial to the flow and solidification behavior of molten metal during the soldering process. In addition, the microstructural refinement, improved dispersion of IMC and the subsequent improvement in mechanical performance affirm the viability of this processing microelectronic packaging.

7. Emerging technologies

Recently, rice husk ash (RHA) has emerged as an affordable reinforcing material for metal-matrix composites, especially in developing nations. The option of RHA as reinforcement emanates from its high silica content and the matching low density compared to other traditional ceramics [161–163]. The interfacial IMC layer thickness of the ENImAg solder joints was significantly lower than that of the bare Cu counterparts, according to a comparative investigation [164] on the reliability of RHA-reinforced Sn-0.7Cu composite solder joints formed on bare Cu and ENImAg surface finish. Similar to the bare Cu counterpart, the plain solder/ENImAg junction showed increased shear strength. The exploration of dimple microtextured Cu substrate on the performance of Sn-0.7Cu solder revealed surface texturing as a reliable method for producing outstanding interfacial reaction between solder and Cu substrate. Increased dimple depth led to a drop in wetting angle of solder joint from 36.5° to 35.1° [165].

Due to its subdued standard Gibbs free energy, the Sn-based Pb-free solder can oxidize easily under ambient conditions [166]. It has been generally established that the oxide film on the solder surface can hinder wettability and solderability, hence, affecting the solder joint reliability. Several methods including the use of doping elements [167–171], acid/plasma cleaning [172–174] and the use of flux have been considered to mitigate the oxidation of solder surface and enhance surface reactivity. However, most of these methods are either less efficient or costly to be implemented. Thermocompression bonding technology using micro-nano cones array (MCA) has shown great potentials for fluxless bonding and can achieve bonding in ambient atmosphere at low temperatures (160 °C–200 °C) [175,176].

Fig. 21a shows the schematic for the thermocompression bonding used in preparing the joint of Ni MCA (Fig. 21b) with SAC305 solder ball [177]. The Ni MCA layer was fabricated on

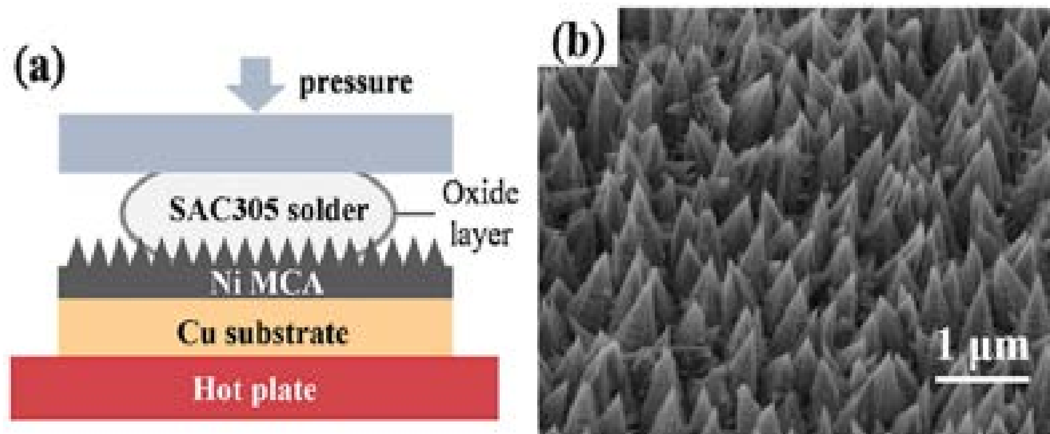

Fig. 21 – (a) Schematic for the bonding process, and (b) Microstructure of Ni MCA employed for bonding [177].

the Cu substrate with the Ni cones having an average height of 700–1000 nm. More so, the Ni MCA was electroplated with a thin Pd layer to decrease the interference of the Ni side at the bonding interface. Ultimately, the local plastic deformation triggered by microcone tips in the course of bonding led to the disintegration of the oxide layer that enabled close metallic contact and thus bonding. The interface was compact and the shear strength did not degrade after aging for 120 h.

Transient liquid phase bonding (TLPB), as compared to other bonding types can significantly reduce the temperature and amount of time needed for effective 3D packaging. Sun et al. [178] studied the microstructure evolution and bonding strength of the Sn-0.3Al solder system as a transient liquid bonding intermediate layer. The submicron Al addition appeared to have slowed the onset of IMC and greatly decreased the frequency of voids in the Sn-0.3Al TLPB joints, thus, improving the reliability of TLPB joints. Additionally, the submicron Al particles greatly increased the spreading area, shear strength, and microhardness of the developed TLPB joints by 69.5%, 45.6%, and 20%, respectively.

A major challenge limiting the full implementation of Sn-based Pb-free solder is its poorer wettability compared to that of the Sn–Pb counterpart. Since the solder wets and spreads on the Cu_6Sn_5 IMC layer during interfacial reaction with the Cu substrate, the higher the surface energy of the Cu_6Sn_5 layer which is strongly associated with its crystal orientation, the greater the wettability of the solder. In essence, a reliable method to improve the wettability of Sn-based Pb-free solder, in particular, without the use of any additives, is to generate a Cu_6Sn_5 coating with high surface energy on the Cu substrate by controlling the crystal orientation. Magnetron sputtering technology was used to create Cu_6Sn_5 preferred-orientation coatings with high surface energies on Cu substrates, with the ability to adjust crystal orientation using its power and substrate temperature [179]. The results of the experiment showed that the preferred orientation of the Cu_6Sn_5 coatings (40–2 and 132) had a significant positive impact on the wettability and wetting dynamics of the SAC305 solder alloy. In the course of exploring the effectiveness of epoxy resin in enhancing the intrinsic properties of SAC305 solder paste, Zhang et al. [180] observed improved spreadability of solder on Cu substrate due to decrease in the surface tension and viscosity of the molten solder by the presence of the epoxy resin. As a result of the mechanical blocking influence of the epoxy resin layer, the shear force of the solder joint increased significantly with the solder having 8 wt% epoxy resin demonstrating the superior value of 35.39 N. Having inspired immense concern among researchers, the superb intrinsic strength and outstanding thermal conductivity of graphene [134,181–183] have been identified as promising solution to the challenges inhibiting the implementation of composite solder systems for industrial applications.

Nevertheless, researches done so far on the preparation of graphene reinforced Sn-based solder using the conventional reflow soldering process have indicated the high possibility of agglomeration occurrence despite the homogenous engulfment of graphene in the solder matrix. Moreover, several reinforcing materials have been detected to float at the topmost part of the matrix by using this technique which in turn deteriorate the mechanical behavior of the solder joints [184,185]. It has been reported that the transient current bonding (TCB) technology can remarkably hinder the agglomeration phenomenon and floating of graphene in the solder matrix during reflow in order to improve the solder joint strength [181,186–188]. In addition, the suitability of TCB for composite soldering also stems from the capacity of the technology to enhance the transformation of scallop-like IMC into dendrites [189,190].

Recently, the lifespan of solder interconnect has been shortened by serious reliability issues of electromigration (EM) and thermomigration (TM) resulting from high-density packaging, increasing chip integration and the reduction of micro-bump size in 3D integrated circuits [181]. In general, the direction of the driving force for EM is from the cathode to the anode in the solder joint, and that for TM is from the hot end to the cold end. When the two directions are the same, the migration of metal atoms will be promoted, otherwise EM flux and TM flux will cancel each other out and atomic migration will be hindered. In view of this, researchers in recent times have focused on boosting the electromigration resistance of micro-joints by microalloying and substrate improvement.

The enhancement of EM resistance by microalloying can be achieved through the addition of Zn and Ag alloying elements

that can react with Sn and Cu atoms to form fine and stable IMCs capable of suppressing the polarity effect and strength reduction caused by current stress [191,192]. The addition of Co has the capacity to tilt the c-axis of Sn grains and increase the angle between the c axis and the current direction [193]. Therefore, Cu atom diffusion in Sn and the growth of interfacial IMCs are inhibited and the EM life of the solder joint can be improved. The ability of rare earth elements such as Ge and Ce to aggregate at the grain boundaries make them inhibit grain boundary slip and dislocation movement, which improves the EM resistance of solder joint [194,195].

Recently, a new MEIMC has been explored at the interface between Sn-rich solders and multielement alloys (MEAs) lying between medium and high-entropy alloys [196–198]. It exhibited excellent thermal stability during thermal aging, which can be attributed to the good thermal stability and slow diffusion of the MEA substrate. Among MEAs, the FeCoNiMn alloy (FCNM) has shown excellent wettability with Sn-based solders, forming a super thin (Fe, Co, Ni, Mn)Sn_2 IMC at the interface [199]. Shen et al. [200] investigated thermomigration in Cu/Sn3.5Ag/FCNM solder joints between a cold end (50 °C) and a hot end (200 °C) at different times. The rapid thickenening of the multielement intermetallic compound (MEIMC), (Cu, Mn, Fe, Co, Ni)$_6Sn_5$ at the Sn3.5Ag/FCNM interface was curtailed by the low chemical flux from FCNM, thereby causing a replacement by Cu_6Sn_5 formation near the Cu/Sn3.5Ag interface. Hence, the system has been proposed as a promising diffusion barrier for thermomigration in micro solder joints.

8. Concluding remarks

In the last decade, a great number of researches have been explored to make clear the reliability progression of Sn-based lead free solders subjected to various unique environments through the exploration of several novel techniques for the preparation of the solder joints. Numerous efforts have been directed towards the utilization of ENImAg surface finish to enhance the reliability of the Sn-based solder joints. Besides the economic viability of producing the ENImAg substrate, the elimination of the black line nickel solder joint defect common with ENIG substrate corroborates the viability of the ENImAg for advanced packaging technologies. Meanwhile, it is important to note that the 3D continuous network structure of interlayer materials can not only remarkably refine the solder microstructure, but also strengthen the mechanical performance, thermal conductivity and overall reliability of the solder. Even though, reliability enhancement could be achieved in solder joints doped with geopolymer ceramics, the composite solder systems are still stuck in the realm of academic research and are quite far from industrial exploitation due to difficulty in controlling the development of composite solders with homogenous composition. Moreover, it may be significant to explore the TCB technology for composite soldering which is viewed as an effective technique to prevent the agglomeration and floating of reinforcing materials, especially nano-sized reinforcements. However, it remains unknown whether the high current density and short bonding duration will impact the phase composition grain orientation and slip system. In summary, this review focuses on the current reliability investigations on Sn-based lead-free solder systems and attempts to offer theoretical support for the development of robust interconnection materials for microelectronics packaging. With rapid advancement in electronics technology, more researches on developing novel solder materials or techniques to revamp the existing ones are envisaged to be further explored in order to achieve compliance with the standards of electronics industry in the near future.

Declaration of competing interest

The authors declare that they have no known competing financial interests or personal relationships that could have appeared to influence the work reported in this paper.

Acknowledgement

This work was supported by Tenaga Nasional Berhad (TNB) and UNITEN through the BOLD Refresh Postdoctoral Fellowships under the project code of J510050002-IC-6 BOLDREFRESH2025-Centre of Excellence.

REFERENCES

[1] Yang L, Zhou W, Ma Y, Li X, Liang Y, Cui W, et al. Effects of Ni addition on mechanical properties of Sn58Bi solder alloy during solid-state aging. Mater Sci Eng, A 2016;667:368–75.

[2] Li S, Liu Y, Zhang H, Cai H, Sun F, Zhang G. Microstructure and hardness of SAC305 and SAC305-0.3 Ni solder on Cu, high temperature treated Cu, and graphene-coated Cu substrates. Results Phys 2018;11:617–22.

[3] Cheng J, Hu X, Li Q, Jiang X. Influences of Ni addition into Cu–x Ni alloy on the microstructure evolution and mechanical property of Sn–58Bi/Cu–x Ni solder joint. Appl Phys A 2020;126:1–10.

[4] Zhao M, Zhang L, Liu ZQ, Xiong MY, Sun L, Jiang N, et al. Microstructures and properties of SnAgCu lead-free solders bearing CuZnAl particles. J Mater Sci Mater Electron 2019;30:15054–63.

[5] Lee HB, Kim YW, Kim SH, Park SH, Choi JP, Aranas Jr C. A modular solder system with hierarchical morphology and backward compatibility. Small 2018;14(33):1801349.

[6] Ren G, Collins MN. Improved reliability and mechanical performance of Ag microalloyed Sn58Bi solder alloys. Metals 2019;9(4):462.

[7] Zhang L, Liu ZQ. Inhibition of intermetallic compounds growth at Sn–58Bi/Cu interface bearing CuZnAl memory particles (2–6 μm). J Mater Sci Mater Electron 2020;31:2466–80.

[8] Sun L, Chen MH, Zhang L, Xie LS. Effect of addition of CuZnAl particle on the properties of Sn solder joint. J Mater Process Technol 2020;278:116507.

[9] Zhao M, Zhang L, Sun L, Xiong MY, Jiang N, Xu KK. Effects of nanoparticles on properties and interface reaction of Sn solder for microelectronic packaging. Int J Mod Phys B 2020;34(8):2050064.

[10] Dong MJ, Gao ZM, Liu YC, Wang X, Yu LM. Effect of indium addition on the microstructural formation and soldered

interfaces of Sn-2.5 Bi-1Zn-0.3 Ag lead-free solder. Int J Miner Metall Mater 2012;19:1029–35.

[11] Xiong MY, Zhang L, He P, Long WM. Stress analysis and structural optimization of 3-D IC package based on the Taguchi method. Solder Surf Mt Technol 2020;32(1):42–7.

[12] Shnawah DA, Sabri MFM, Badruddin IA, Said SBM, Ariga T, Che FX. Effect of Ag content and the minor alloying element Fe on the mechanical properties and microstructural stability of Sn-Ag-Cu solder alloy under high-temperature annealing. J Electron Mater 2013;42:470–84.

[13] Huang CY, Huang HH. Process optimization of SnCuNi soldering material using artificial parametric design. J Intell Manuf 2014;25(4):813–23.

[14] Dong G, Tan S, Han J, Wang Y, Guo F, Ma L. Study on slip behavior of lead-free solder joints under uniaxial stress. In2017 18th International Conference on Electronic Packaging Technology (ICEPT) 2017, August:1043–5 [IEEE].

[15] Shalaby RM, Kamal M, Ali EAM, Gumaan MS. Design and properties of new lead-free solder joints using Sn-3.5 Ag-Cu solder. Silicon 2018;10:1861–71.

[16] Guo B, Kunwar A, Zhao N, Chen J, Wang Y, Ma H. Effect of Ag3Sn nanoparticles and temperature on Cu6Sn5 IMC growth in Sn-xAg/Cu solder joints. Mater Res Bull 2018;99:239–48.

[17] Hasnine M, Vahora N. Microstructural and mechanical behavior of SnCu–Ge solder alloy subjected to high temperature storage. J Mater Sci Mater Electron 2018;29(11):8904–13.

[18] Gupta A, Srivastava C. Correlation between microstructure and corrosion behaviour of SnBi-graphene oxide composite coatings. Surf Coating Technol 2019;375:573–88.

[19] Zhang Z, Hu X, Jiang X, Li Y. Influences of mono-Ni (P) and dual-Cu/Ni (P) plating on the interfacial microstructure evolution of solder joints. Metall Mater Trans 2019;50:480–92.

[20] Xiong MY, Zhang L. Interface reaction and intermetallic compound growth behavior of Sn-Ag-Cu lead-free solder joints on different substrates in electronic packaging. J Mater Sci 2019;54(2):1741–68.

[21] Tao QB, Benabou L, Van TN, Nguyen-Xuan H. Isothermal aging and shear creep behavior of a novel lead-free solder joint with small additions of Bi, Sb and Ni. J Alloys Compd 2019;789:183–92.

[22] Tan AT, Tan AW, Yusof F. Evolution of microstructure and mechanical properties of Cu/SAC305/Cu solder joints under the influence of low ultrasonic power. J Alloys Compd 2017;705:188–97.

[23] Marques VMF, Johnston C, Grant PS. Microstructural evolution at Cu/Sn–Ag–Cu/Cu and Cu/Sn–Ag–Cu/Ni–Au ball grid array interfaces during thermal ageing. J Alloys Compd 2014;613:387–94.

[24] Subramanian KN, Frear DR. Issues related to the implementation of Pb-free electronic solders in consumer electronics. Lead-Free Electronic Solders: A Special Issue of the Journal of Materials Science: Materials in Electronics 2007:319–30.

[25] Zhao R, Ma L, Zuo Y, Liu S, Guo F. Retarding electromigration in lead-free solder joints by alloying and composite approaches. J Electron Mater 2013;42:280–7.

[26] Wang YW, Chang CC, Kao CR. Minimum effective Ni addition to SnAgCu solders for retarding Cu3Sn growth. J Alloys Compd 2009;478(1–2):L1–4.

[27] Wang CH, Huang SE, Li KT. Inhibiting CoSn3 growth at the Sn/Co system by minor Zn addition. Intermetallics 2015;56:68–74.

[28] Zhang R, Xu G, Wang X, Guo F, Lee A, Subramanian KN. Electromigration in Sn-Bi Modified with polyhedral oligomeric silsesquioxane. J Electron Mater 2010;39:2513–21.

[29] Rhee H, Guo F, Lee JG, Chen KC, Subramanian KN. Effects of intermetallic morphology at the metallic particle/solder interface on mechanical properties of Sn-Ag-based solder joints. J Electron Mater 2003;32:1257–64.

[30] Guo F, Xu G, He H. Electromigration behaviors in Sb particle-reinforced composite eutectic SnAgCu solder joints. J Mater Sci 2009;44:5595–601.

[31] Dele-Afolabi TT, Hanim MA, Ojo-Kupoluyi OJ, Calin R. Impact of different isothermal aging conditions on the IMC layer growth and shear strength of MWCNT-reinforced Sn–5Sb solder composites on Cu substrate. J Alloys Compd 2019;808:151714.

[32] Dele-Afolabi TT, Hanim MA, Calin R, Ilyas RA. Microstructure evolution and hardness of MWCNT-reinforced Sn-5Sb/Cu composite solder joints under different thermal aging conditions. Microelectron Reliab 2020;110:113681.

[33] Ma Y, Li X, Zhou W, Yang L, Wu P. Reinforcement of graphene nanosheets on the microstructure and properties of Sn58Bi lead-free solder. Mater Des 2017;113:264–72.

[34] Sun L, Zhang L, Zhang Y, Xu YX, Zhang PX, Liu QH, et al. Interfacial reaction and properties of Sn0. 3Ag0. 7Cu containing nano-TiN solder joints. J Mater Sci Mater Electron 2022:1–11.

[35] Reddy BP, Mallikarjuna K, Kumar M, Sekhar MC, Suh Y, Park SH. Highly porous metal organic framework derived NiO hollow spheres and flowers for oxygen evolution reaction and supercapacitors. Ceram Int 2021;47(3):3312–21.

[36] Liu X, Yu H, Shi Z, Huang L, Xia T, Guo R. Porous metal model for calculating slot thermal conductivity coefficient of electric machines. Appl Therm Eng 2017;111:981–8.

[37] Xiong B, Lu H, Bi Y, Huang J, He S. Shear strength of joint formed using Sn-58Bi/Cu porous structure via TLP bonding. In: MEMAT 2022; 2nd international *Conference on mechanical engineering, intelligent Manufacturing and automation technology*. VDE; 2022, January. p. 1–4.

[38] Wang J, Wang H, Lv Z, Zhong X, Mao X, Chen H. A high-remelting-point interconnect method based on porous copper and Sn42Bi58 solder. In: 2022 23rd international confer*ence on electronic packaging technology (ICEPT)*. IEEE; 2022, August. p. 1–4.

[39] Choi H, Kim CL, Sohn Y. Diffusion barrier properties of the intermetallic compound layers formed in the Pt nanoparticles alloyed Sn-58Bi solder joints reacted with ENIG and ENEPIG surface finishes. Materials 2022;15(23):8419.

[40] Wang J, Sun Q, Tang XX, Wang XN, Akira K. Influence mechanism of Au layer thickness on wettability of Sn–Ag–Cu solder on heated ENIG pads. Vacuum 2022;201:111074.

[41] Rajendran SH, Jung DH, Jung JP. Investigating the physical, mechanical, and reliability study of high entropy alloy reinforced Sn–3.0 Ag–0.5 Cu solder using 1608 chip capacitor/ENIG joints. J Mater Sci Mater Electron 2022;33(7):3687–710.

[42] Said RM, Ghani MAHA, Saud N, Salleh MAAM. Microstructure evolution of Sn-Cu based solder paste on electroless nickel immersion gold (ENIG) surface finish subjected to multiple reflow cycles. In: AIP conference proceedings, vol. 2347. AIP Publishing LLC; 2021, July. p. 020194.

[43] Tian R, Tian Y, Huang Y, Yang D, Chen C, Sun H. Comparative study between the Sn–Ag–Cu/ENIG and Sn–Ag–Cu/ENEPIG solder joints under extreme temperature thermal shock. J Mater Sci Mater Electron 2021;32:6890–9.

[44] Azmah Hanim MA, Wei CK, Dele-Afolabi TT, Azlina OS. Shear analysis of rice husk ash (RHA) reinforced tin-0.7-copper composite solders on electroless nickel/immersion silver (ENIAg) surfaces. Mater Werkst 2021;52(9):943–51.
[45] Zolhafizi J, Azlina OS. The influence of Copper and Bismuth element in Sn-Ag solders and ENIMAG substrate. IOP Conf Ser Mater Sci Eng 2019, December;701(No. 1):12012 [IOP Publishing].
[46] Liew YM, Heah CY, Li LY, Jaya NA, Abdullah MMAB, Tan SJ, et al. Formation of one-part-mixing geopolymers and geopolymer ceramics from geopolymer powder. Construct Build Mater 2017;156:9–18.
[47] Koleżyński A, Król M, Żychowicz M. The structure of geopolymers theoretical studies. J Mol Struct 2018;1163:465–71.
[48] Mohamed R, Abd Razak R, Abdullah MMAB, Shuib RK, Ahmad R, Aziz IH, et al. Heat evolution of class C fly ash geopolymers with different molarity of sodium hydroxide: nucleation growth and morphology properties towards early strength evaluation. IOP Conf Ser Mater Sci Eng 2020, May;864(No. 1):12008 [IOP Publishing].
[49] Jamil NH, Abdullah MMAB, Pa FC, Mohamad H, Ibrahim WMAW, Amonpattaratkit P, …, Ibrahim N. Self-fluxing mechanism in geopolymerization for low-sintering temperature of ceramic. Materials 2021;14(6):1325.
[50] Zaimi NSM, Ramli MII, Salleh MAAM, Abdullah MMAB, Chaiprapa J, Aziz MSA. Synthesis of kaolin geopolymer as ceramic reinforcement in lead-free solder. J Phys Conf 2022;2169(No. 1):012019 [IOP Publishing].
[51] Zhang YH, Räbiger D, Eckert S. Solidification of pure aluminium affected by a pulsed electrical field and electromagnetic stirring. J Mater Sci 2016;51:2153–9.
[52] Nagira T, Nakatsuka N, Yasuda H, Uesugi K, Takeuchi A, Suzuki Y. Impact of melt convection induced by ultrasonic wave on dendrite growth in Sn–Bi alloys. Mater Lett 2015;150:135–8.
[53] Hammad AE, El-Molla S, Ragab M. Impact of rotating magnetic field on the microstructure, thermal properties, and creep behavior during the solidification of Sn–2.0 Ag–0.5 Cu solder alloy. Proc Inst Mech Eng Part L 2023;237(2):317–28.
[54] Zhang P, Xue S, Wang J, Xue P, Zhong S, Long W. Effect of nanoparticles addition on the microstructure and properties of lead-free solders: a review. Appl Sci 2019;9(10):2044.
[55] Sahrudin IN, Aziz MSA, Abdullah MZ, Salleh MAAM. Study on the addition of nanoparticles in the lead-free solder during reflow soldering via numerical simulation-a review. CFD Lett 2020;12(5):111–9.
[56] Li ML, Zhang L, Jiang N, Zhang L, Zhong SJ. Materials modification of the lead-free solders incorporated with micro/nano-sized particles: a review. Mater Des 2021;197:109224.
[57] Efzan ME, Haslinda MN, Abdullah MAB. A review: effect of nanoparticles addition on the properties of Sn-Ag-Cu lead free solder alloy. In: AIP conference proceedings, vol. 2347. AIP Publishing LLC; 2021, July. p. 020078.
[58] Efzan E, Abdalla H, Nirmal U. Review on the Al2O3 nanoparticle reinforcement effect on thermal and mechanical properties of SAC alloys. In: AIP conference proceedings, vol. 2347. AIP Publishing LLC; 2021, July. p. 020073.
[59] Bharath Krupa Teja M, Sharma A, Das S, Das K. A review on nanodispersed lead-free solders in electronics: synthesis, microstructure and intermetallic growth characteristics. J Mater Sci 2022;57(19):8597–633.
[60] Page MJ, McKenzie JE, Bossuyt PM, Boutron I, Hoffmann TC, Mulrow CD, et al. The PRISMA 2020 statement: an updated guideline for reporting systematic reviews. Int J Surg 2021;88:105906.
[61] Comisso N, Cattarin S, Guerriero P, Mattarozzi L, Musiani M, Vázquez-Gómez L, et al. Study of Cu, Cu-Ni and Rh-modified Cu porous layers as electrode materials for the electroanalysis of nitrate and nitrite ions. J Solid State Electrochem 2016;20(4):1139–48.
[62] Wang L, Wang X, Meng Z, Hou H, Chen B. MOF-templated thermolysis for porous CuO/Cu2O@ CeO2 anode material of lithium-ion batteries with high rate performance. J Mater Sci 2017;52(12):7140–8.
[63] Zaharinie T, Moshwan R, Yusof F, Hamdi M, Ariga T. Vacuum brazing of sapphire with Inconel 600 using Cu/Ni porous composite interlayer for gas pressure sensor application. Mater Des 2014;54:375–81. 1980-2015.
[64] El-Hadek MA, Kaytbay S. Mechanical and physical characterization of copper foam. Int J Mech Mater Des 2008;4:63–9.
[65] Chen F, Chen C, Hu Q, Xiang B, Song T, Zou X, …, Deng M. Synthesis of CuO@ CoNi LDH on Cu foam for high-performance supercapacitors. Chem Eng J 2020;401:126145.
[66] Zhu ZW, Wang ZY, Liu S, Li GR, Gao XP. Uniform lithium plating within 3D Cu foam enabled by Ag nanoparticles. Electrochim Acta 2021;379:138152.
[67] Bidault F, Brett DJL, Middleton PH, Abson N, Brandon NP. A new application for nickel foam in alkaline fuel cells. Int J Hydrogen Energy 2009;34(16):6799–808.
[68] Chaudhari NK, Jin H, Kim B, Lee K. Nanostructured materials on 3D nickel foam as electrocatalysts for water splitting. Nanoscale 2017;9(34):12231–47.
[69] Obodo RM, Shinde NM, Chime UK, Ezugwu S, Nwanya AC, Ahmad I, …, Ezema FI. Recent advances in metal oxide/hydroxide on three-dimensional nickel foam substrate for high performance pseudocapacitive electrodes. Current Opinion in Electrochemistry 2020;21:242–9.
[70] Brothers AH, Dunand DC. Mechanical properties of a density-graded replicated aluminum foam. Mater Sci Eng, A 2008;489(1–2):439–43.
[71] He SY, Zhang Y, Dai G, Jiang JQ. Preparation of density-graded aluminum foam. Mater Sci Eng, A 2014;618:496–9.
[72] Yu H, Chen H, Pan M, Tang Y, Zeng K, Peng F, et al. Effect of the metal foam materials on the performance of methanol steam micro-reformer for fuel cells. Appl Catal Gen 2007;327(1):106–13.
[73] Zhang C, Zhou W, Wang Q, Wang H, Tang Y, Hui KS. Comparison of static contact angle of various metal foams and porous copper fiber sintered sheet. Appl Surf Sci 2013;276:377–82.
[74] Liu K, Li Y, Xia C, Wang J. Microstructural evolution and properties of TLP diffusion bonding super-Ni/NiCr laminated composite to Ti-6Al-4V alloy with Cu interlayer. Mater Des 2017;135:184–96.
[75] Aboudi D, Lebaili S, Taouinet M, Zollinger J. Microstructure evolution of diffusion welded 304L/Zircaloy4 with copper interlayer. Mater Des 2017;116:386–94.
[76] Zahri NAM, Yusof F, Miyashita Y, Ariga T, Haseeb AMA, Jamadon NH, et al. Brazing of porous copper foam/copper with amorphous Cu-9.7 Sn-5.7 Ni-7.0 P (wt%) filler metal: interfacial microstructure and diffusion behavior. Weld World 2020;64(1):209–17.
[77] Shirzadi AA, Zhu Y, Bhadeshia HKDH. Joining ceramics to metals using metallic foam. Mater Sci Eng, A 2008;496(1–2):501–6.

[78] Guo W, Xue J, Zhang H, Cui H, Zhu Y, Peng P, et al. The role of foam on microstructure and strength of the brazed C/C composites/Ti6Al4V alloy joint. Vacuum 2020:109543.
[79] Lei L, He X, Xing B, Zhao D, Gu F, Ball A. Effect of foam copper interlayer on the mechanical properties and fretting wear of sandwich clinched joints. J Mater Process Technol 2019;274:116285.
[80] Liu Y, Ren B, Zhou M, Zeng X, Sun F. Microstructure, mechanical, and thermal behaviors of SnBi/Cu solder joint enhanced by porous Cu. J Mater Sci Mater Electron 2020;31(11):8258–67.
[81] Liu Y, Ren B, Xu R, Zhang H, Sun F. Effect of porous Cu addition on the microstructure and properties of Sn58Bi solder joints. Mater Res Express 2019;6(11):116301.
[82] Liu Y, Ren B, Xue Y, Zhou M, Cao R, Zeng X. Improvement on the mechanical properties of eutectic Sn58Bi alloy with porous Cu addition during isothermal aging. Mater Res Express 2021;8(7):076302.
[83] Liu Y, Ren B, Zhou M, Xue Y, Zeng X, Sun F, et al. Effect of porous Cu addition on the microstructure and mechanical properties of SnBi-xAg solder joints. Appl Phys A 2020;126(9):1–10.
[84] Liu Y, Ren B, Xue Y, Zhou M, Cao R, Chen P, et al. Microstructure and mechanical behavior of SnBi-xAg and SnBi-xAg@ P-Cu solder joints during isothermal aging. Microelectron Reliab 2021;127:114388.
[85] Liu Y, Ren B, Xue Y, Zhou M, Cao R, Chen P, et al. Pressure-assisted soldering of copper using porous metal-reinforced Sn58Bi solder. J Mater Sci Mater Electron 2021;32(14):18968–77.
[86] Jamadon NH, Tan AW, Yusof F, Ariga T, Miyashita Y, Hamdi M. Utilization of a porous Cu interlayer for the enhancement of Pb-Free Sn-3.0 Ag-0.5 Cu Solder joint. Metals 2016;6(9):220.
[87] Hani JN, Fadzil JM, Farazila Y, Tadashi A, Yukio M, Hamdi AM. The effect of temperature on the formation behavior of reaction layer in Sn-3.0 Ag-0.5 Cu solder joint with the addition of porous Copper interlayer: der Einfluss der Temperatur auf das Bildungsverhalten der Reaktionsschicht in der Sn-3, 0Ag-0, 5Cu-Lötverbindung mit einer porösen Kupfer-Zwischenschicht. Mater Werkst 2017;48(3–4):283–9.
[88] Jamadon NH, Yusof F, Shukor MAH, Ariga T, Miyashita Y. Addition of porous Cu interlayer to Sn-3.0 Ag-0.5 Cu lead-free solder joint for high temperature application. In: 36th international electronics *manufacturing technology conference*. IEEE; 2014, November. p. 1–5.
[89] Jamadon NH, Ahmad ND, Yusof F, Ariga T, Miyashita Y, Shukor MHA. Effect of isothermal aging on mechanical properties of Sn-3.0 Ag-0.5 Cu solder alloy with porous Cu interlayer addition. In: 2nd international conference on mechanical, manufacturing and process plant engineering. Singapore: Springer; 2017. p. 59–67.
[90] Jamadon NH, Miyashita Y, Yusof F, Hamdi M, Otsuka Y, Ariga T. Formation behaviour of reaction layer in Sn-3.0 Ag-0.5 Cu solder joint with addition of porous Cu interlayer. IOP Conf Ser Mater Sci Eng 2014, August;61(No. 1):12020 [IOP Publishing].
[91] Hanim MA, Dasan AB, Dele-Afolabi TT, Ariga T, Vidyatharran K. Influence of porous Cu interlayer on the intermetallic compound layer and shear strength of MWCNT-reinforced SAC 305 composite solder joints. J Mater Sci Mater Electron 2021;32(4):4515–28.
[92] Yi X, Zhang R, Hu X. Study on the microstructure and mechanical property of Cu-foam modified Sn3. 0Ag0. 5Cu solder joints by ultrasonic-assisted soldering. J Manuf Process 2021;64:508–17.
[93] Kim SW, Son KT, Hyun SK. Mechanical behaviors of lotus-type porous Cu/Cu joint soldered by Sn-3.0 Ag-0.5 Cu alloy. Mater Sci Eng, A 2021;822:141655.
[94] Su Y, Hang C, Chen H, Xie X, Ma J, Li M. Interconnection method based on solder-filled nanoporous copper as interlayer for high-temperature applications. Microelectron Eng 2019;214:60–7.
[95] Koga S, Nishikawa H, Saito M, Mizuno J. Fabrication of nanoporous Cu sheet and application to bonding for high-temperature applications. J Electron Mater 2020;49(3):2151–8.
[96] He H, Huang S, Ye Y, Xiao Y, Zhang Z, Li M, et al. Microstructure and mechanical properties of Cu joints soldered with a Sn-based composite solder, reinforced by metal foam. J Alloys Compd 2020;845:156240.
[97] He H, Huang S, Xiao Y, Goodall R. Diffusion reaction-induced microstructure and strength evolution of Cu joints bonded with Sn-based solder containing Ni-foam. Mater Lett 2020;281:128642.
[98] Wang Q, Xiao Y, Zhang X. Ultrasound-assisted soldering of Cu alloy using a Ni-foam reinforced Sn composite solder. In: 2017 18th international conf*erence on electronic packaging technology (ICEPT)*. IEEE; 2017, August. p. 875–8.
[99] Xiao Y, Wang Q, Wang L, Zeng X, Li M, Wang Z, …, Zhu X. Ultrasonic soldering of Cu alloy using Ni-foam/Sn composite interlayer. Ultrason Sonochem 2018;45:223–30.
[100] Xiao Y, Li S, Wang Z, Song Z, Mao Y, Li M. Microstructure and mechanical properties of 7075-Al alloy joint ultrasonically soldered with Ni-foam/Sn composite solder. Mater Sci Eng, A 2018;729:241–8.
[101] Niu W, Xiao Y, Wan C, Li D, Fu H, He H. Ultrasonic bonding of 2024 Al alloy using Ni-foam/Sn composite solder at ambient temperature. Mater Sci Eng, A 2020;771:138663.
[102] He H, Song L, Gao H, Xiao Y, Cao Y. Microstructure evolution and grain refinement of ultrasonic-assisted soldering joint by using Ni foam reinforced Sn composite solder. Ultrason Sonochem 2023;92:106244.
[103] Namazu T, Ohtani K, Inoue S, Miyake S. Influences of exothermic reactive layer and metal interlayer on fracture behavior of reactively bonded solder joints. J Eng Mater Technol 2015;137(3).
[104] Geim AK, Novoselov KS. The rise of graphene. Nat Mater 2007;6(3):183–91.
[105] Fan YC, Wang LJ, Li JL, Li JQ, Sun SK, Chen F, …, Jiang W. Recent progress in graphene based ceramic composites. Carbon 2010;48(6):1743–9.
[106] Ramirez C, Garzón L, Miranzo P, Osendi MI, Ocal C. Electrical conductivity maps in graphene nanoplatelet/silicon nitride composites using conducting scanning force microscopy. Carbon 2011;49(12):3873–80.
[107] Wang K, Wang Y, Fan Z, Yan J, Wei T. Preparation of graphene nanosheet/alumina composites by spark plasma sintering. Mater Res Bull 2011;46(2):315–8.
[108] Chen S, Brown L, Levendorf M, Cai W, Ju SY, Edgeworth J, …, Ruoff RS. Oxidation resistance of graphene-coated Cu and Cu/Ni alloy. ACS Nano 2011;5(2):1321–7.
[109] Yang W, Zhou J, Jiang X, Ye X, Xuan X, Wu C, et al. Cu-Cu low temperature bonding based on lead-free solder with graphene interlayer. Appl Phys Lett 2019;115(12):122102.
[110] Ko YH, Lee JD, Yoon T, Lee CW, Kim TS. Controlling interfacial reactions and intermetallic compound growth at the interface of a lead-free solder joint with layer-by-layer transferred graphene. ACS Appl Mater Interfaces 2016;8(8):5679–86.
[111] Yin X, Wu C, Zhang Z, Yang W, Xie C, Yang X, et al. Highly reliable CuCu low temperature bonding using SAC305 solder with rGO interlayer. Microelectron Reliab 2022;129:114483.

[112] Wang H, Leong WS, Hu F, Ju L, Su C, Guo Y, …, Kong J. Low-temperature copper bonding strategy with graphene interlayer. ACS Nano 2018;12(3):2395–402.
[113] Bader S, Gust W, Hieber H. Rapid formation of intermetallic compounds interdiffusion in the Cu; Sn and Ni; Sn systems. Acta Metall Mater 1995;43(1):329–37.
[114] Liang MW, Hsieh TE, Chang SY, Chuang TH. Thin-film reactions during diffusion soldering of Cu/Ti/Si and Au/Cu/Al2O3 with Sn interlayers. J Electron Mater 2003;32(9):952–6.
[115] Lin YF, Hao YC, Ouyang FY. Improvement of thermomigration resistance in lead-free Sn3. 5Ag alloys by Ag interlayer. J Alloys Compd 2020;847:156429.
[116] Long E, Toscano L. Electroless Nickel/Immersion Silver—a new surface finish PCB applications. Met Finish 2013;111(1):12–9.
[117] Milad G. Is "black pad" still an issue for ENIG? Circuit World; 2010.
[118] Adawiyah MR, Azlina OS. Comparative study on the isothermal aging of bare Cu and ENImAg surface finish for Sn-Ag-Cu solder joints. J Alloys Compd 2018;740:958–66.
[119] Rabiatul Adawiyah MA, Amirul SA, Saliza Azlina O, Syafiq H. Impact of multiple reflow on intermetallic compound of nickel-doped tin-silver-copper on ENImAg substrate. Mater Werkst 2020;51(6):780–6.
[120] Yoon JW, Jung SB. Interfacial reactions between Sn–0.4 Cu solder and Cu substrate with or without ENIG plating layer during reflow reaction. J Alloys Compd 2005;396(1–2):122–7.
[121] Liu P, Yao P, Liu J. Effects of multiple reflows on interfacial reaction and shear strength of SnAgCu and SnPb solder joints with different PCB surface finishes. J Alloys Compd 2009;470(1–2):188–94.
[122] Anuar RAM, Hamidin MS, Osman SA, Othman MH. Intermetallic compound layer growth at the interface between Sn-Ag and ENImAg surface finish. Int J 2020;8(1.2).
[123] Adawiyah MR, Azlina OS. Solder volume effect on interfacial reaction between Sn-Ag-Cu/ENImAg substrate. Procedia Eng 2017;184:604–10.
[124] Li W. Failure analysis on bad wetting of ENIG surface finish pads. In: 2015 16th international conf*erence on electronic packaging technology (ICEPT)*. IEEE; 2015, August. p. 538–41.
[125] Zhengrong C, Jianwei Z, Xingming F, Jaisung L. Pad finish related board-level solder joint reliability research. In: 2010 11th international conf*erence on electronic packaging technology & high density packaging*. IEEE; 2010, August. p. 1039–42.
[126] Toscano LM, Long E. A new surface finish for the electronics industry: electroless nickel/immersion silver. In: 2014 9th international microsy*stems, packaging, Assembly and circuits technology conference (IMPACT)*. IEEE; 2014, October. p. 372–8.
[127] Arra M, Shangguan D, Xie D, Sundelin J, Lepistö T, Ristolainen E. Study of immersion silver and tin printed-circuit-board surface finishes in lead-free solder applications. J Electron Mater 2004;33:977–90.
[128] Adawiyah MR, Azlina OS. Interfacial reaction between SAC305 lead–free solders and ENImAg surface finish and bare copper: grenzflächenreaktion zwischen bleifreien Lötmetallen SAC305 und ENImAg-Oberflächenfinish und blankem Kupfer. Mater Werkst 2017;48(3–4):235–40.
[129] Mohamed Anuar RA, Osman SA. The formation of intermetallic layer structure of SAC405/Cu and SAC405/ENImAg solder joint interfaces. Solder Surf Mt Technol 2021;33(2):75–85.
[130] Rabiatul Adawiyah MA, Hafiz ABM, Saliza Azlina O, Zolhafizi J, Wan Nur Azrina WM, Shahrul Azmir O. The effect of cooling rate during multiple reflow soldering on intermetallic layer of Sn-4.0 Ag-0.5 Cu/ENImAg. Mater Werkst 2019;50(3):295–301.
[131] Zolhafizi J, Azlina S. The effect of Bismuth on intermetallics growth between lead-free solders and electroless nickel immersion silver (ENIMAG) surface Finish. Key Eng Mater 2019;796:183–8 [Trans Tech Publications Ltd].
[132] Vidyatharran K, Hanim MA, Dele-Afolabi TT, Matori KA, Azlina OS. Microstructural and shear strength properties of GNSs-reinforced Sn-1.0 Ag-0.5 Cu (SAC105) composite solder interconnects on plain Cu and ENIAg surface finish. J Mater Res Technol 2021;15:2497–506.
[133] Dele-Afolabi TT, Hanim MA, Vidyatharran K, Matori KA, Azlina OS, Calin R. Interfacial microstructure evolution and shear strength of MWCNTs-reinforced Sn-1.0 Ag-0.5 Cu (SAC105) composite solder interconnects on plain Cu and ENIAg surface finish. J Mater Sci Mater Electron 2022;33(10):8233–46.
[134] Liu XD, Han YD, Jing HY, Wei J, Xu LY. Effect of graphene nanosheets reinforcement on the performance of Sn; Ag; Cu lead-free solder. Mater Sci Eng, A 2013;562:25–32.
[135] Jung DH, Sharma A, Jung JP. Influence of dual ceramic nanomaterials on the solderability and interfacial reactions between lead-free Sn-Ag-Cu and a Cu conductor. J Alloys Compd 2018;743:300–13.
[136] Mostapha M, Salleh MAAM, Abdullah MMAB, Thiaghu M, Zaimi NSM, Ahmad R. Characterization of geopolymer ceramic reinforced Sn-0.7 Cu composite solder: effect of milling time and speed. IOP Conf Ser Mater Sci Eng 2019, December;701(No. 1):12016 [IOP Publishing].
[137] Somidin F, Ilias NFN, Zaimi NSM, Ramli MII, Razak NRA. Influence of fly ash geopolymer ceramic powder addition on Sn-3.0 Ag-0.5 Cu solder joints. J Phys Conf 2022;2169(No. 1):012032 [IOP Publishing].
[138] Zulkifli NNIB, Abdullah MMAB, Salleh MAAM. Fabrication of novel geopolymer reinforced tin copper solder in suppressing intermetallic layer growth. IOP Conf Ser Mater Sci Eng 2019, August;551(No. 1):12091 [IOP Publishing].
[139] Zaimi NSM, Salleh MAAM, Abdullah MMAB, Mostapha M, Ahmad R. Influence of kaolin geopolymer ceramic additions to the wettability and electrical properties of Sn-3.0 Ag-0.5 Cu (SAC305) lead free solder. IOP Conf Ser Mater Sci Eng 2019, December;701(No. 1):12033 [IOP Publishing].
[140] Zulkifli NI, Abdullah MMAB, Salleh MAAM, Ahmad R, Sandu AV, Mortar NAM. Development of geopolymer ceramic as a potential reinforcing material in solder alloy: short review. IOP Conf Ser Mater Sci Eng 2020, February;743(No. 1):12023 [IOP Publishing.].
[141] Zaimi NSM, Salleh MAAM, Abdullah MMAB, Mostapha M, Ahmad R. The effect of geopolymer ceramic additions to the wettability and shear strength of Sn-Ag-Cu (SAC) solder: a preliminary study. IOP Conf Ser Mater Sci Eng 2019, August;551(No. 1):12081 [IOP Publishing].
[142] Izzati ZN, Al-Bakri AM, Salleh MM, Ahmad R, Mortar NAM, Ramasamy S. Microstructure and mechanical properties of geopolymer ceramic reinforced Sn-0.7 Cu solder. IOP Conf Ser Mater Sci Eng 2020, May;864(No. 1):12041 [IOP Publishing].
[143] Zaimi NM, Salleh MM, Abdullah MMAB, Ahmad R, Mostapha M, Yoriya S, et al. Effect of kaolin geopolymer ceramic addition on the properties of Sn-3.0 Ag-0.5 Cu solder joint. Mater Today Commun 2020;25:101469.
[144] Zaimi NSM, Salleh MAAM, Abdullah MMAB, Nadzri NIM, Sandu AV, Vizureanu P, …, Sandu IG. Effect of kaolin geopolymer ceramics addition on the microstructure and shear strength of Sn-3.0 Ag-0.5 Cu solder joints during multiple reflow. Materials 2022;15(8):2758.
[145] Zaimi NSM, Salleh MAAM, Sandu AV, Abdullah MMAB, Saud N, Rahim SZA, …, Ramli MII. Performance of Sn-3.0 Ag-0.5 Cu composite solder with kaolin geopolymer ceramic reinforcement on microstructure and mechanical

properties under isothermal ageing. Materials 2021;14(4):776.
[146] Samanta Deep, Zabaras Nicholas. Control of macrosegregation during the solidification of alloys using magnetic fields. Int J Heat Mass Tran 2006;25–26:4850–66.
[147] Travnikov V, Eckert K, Nikrityuk PA, Odenbach S, Vogt T, Eckert S. Flow oscillations driven by a rotating magnetic field in liquid metal columns with an upper free surface. J Cryst Growth 2012;339(1):52–60.
[148] Liu KM, Lu DP, Zhou HT, Chen ZB, Atrens A, Lu L. Influence of a high magnetic field on the microstructure and properties of a Cu–Fe–Ag in situ composite. Mater Sci Eng, A 2013;584:114–20.
[149] Huang M, Zhang Q, Qi L, Deng L, Li Y. Effect of external magnetic field on resistance spot welding of aluminum alloy AA6061-T6. J Manuf Process 2020;50:456–66.
[150] Zeng J, Chen W, Yan W, Yang Y, McLean A. Effect of permanent magnet stirring on solidification of Sn-Pb alloy. Mater Des 2016;108:364–73.
[151] Wang XD, Li TJ, Fautrelle Y, Dupouy MD, Jin JZ. Two kinds of magnetic fields induced by one pair of rotating permanent magnets and their application in stirring and controlling molten metal flows. J Cryst Growth 2005;275(1–2):e1473–9.
[152] El-Daly AA, Ibrahiem AA. Assessment of room-temperature short-term stress relaxation and strain relaxation with recovery in Sn-Bi lead-free solders solidified under rotating magnetic field. J Alloys Compd 2018;730:47–56.
[153] El-Daly AA, Ibrahiem AA. Influence of rotating magnetic field on solidification microstructure and tensile properties of Sn-Bi lead-free solders. Microelectron Reliab 2018;81:352–61.
[154] Grants I, Gerbeth G. Stability of axially symmetric flow driven by a rotating magnetic field in a cylindrical cavity. J Fluid Mech 2001;431:407–26.
[155] El-Taher AM, Abd El Azeem SE, Ibrahiem AA. Novel low Ag-content Sn–Ag–Cu–Sb–Al solder alloys with enhanced elastic compliance and plastic energy dissipation ability by applying rotating magnetic field. J Mater Sci Mater Electron 2021;32:6199–213.
[156] Hammad AE, El-Molla S, Abd El-Rehim AF, Ragab M. Progress on microstructure features and creep properties of prospective Tin-Silver-Zinc alloy using a magnetic field. Mater Res Express 2021;8(8):086506.
[157] Hammad AE, Ragab M. Achieving microstructure refinement and superior mechanical performance of Sn-2.0 Ag-0.5 Cu-2.0 Zn (SACZ) solder alloy with rotary magnetic field. Microelectron Reliab 2020;113:113932.
[158] Hammad AE, Ragab M. Advancement solidification microstructure and mechanical properties of Sn–2.0 Ag–0.5 Cu alloy by applying a rotary magnetic field. J Mater Sci Mater Electron 2019;30:18838–47.
[159] Wang Z, Liu F, Liu J, Zhou J, Wang Z, Yan N. Influences of rotating magnetic field on microstructure and properties of Sn–Ag–Cu–Sb–Ce solder alloy. J Mater Sci Mater Electron 2023;34(6):504.
[160] Kaya H, Çadırlı E, Gündüz M, Raebiger D, Eckert S. Dependency of structure, mechanical and electrical properties on rotating magnetic field in the Bi–Sn–Ag ternary eutectic alloy. Int J Mater Res 2016;107(4):362–71.
[161] Alaneme KK, Sanusi KO. Microstructural characteristics, mechanical and wear behaviour of aluminium matrix hybrid composites reinforced with alumina, rice husk ash and graphite. Engineering Science and Technology, an International Journal 2015;18(3):416–22.
[162] Prasad DS, Shoba C. Hybrid composites–a better choice for high wear resistant materials. J Mater Res Technol 2014;3(2):172–8.
[163] Prasad DS, Shoba C. Experimental evaluation onto the damping behavior of Al/SiC/RHA hybrid composites. J Mater Res Technol 2016;5(2):123–30.
[164] Hanim MA, Kamil NM, Wei CK, Dele-Afolabi TT, Azlina OS. Microstructural and shear strength properties of RHA-reinforced Sn–0.7 Cu composite solder joints on bare Cu and ENIAg surface finish. J Mater Sci Mater Electron 2020;31:8316–28.
[165] Roduan SF, Wahab JA, Salleh MAAM, Mahayuddin NAHM, Abdullah MMAB, Halil ABM, Vizureanu P. Effectiveness of dimple microtextured copper substrate on performance of Sn-0.7 Cu solder alloy. Materials 2022;16(1):96.
[166] Zhang W, Ruythooren W. Characterization of oxidation of electroplated Sn for advanced flip-chip bonding. In 2009 European Microelectronics and Packaging Conference 2009, June:1–4 [IEEE].
[167] Wan Cho S, Han K, Yi Y, Kang SJ, Yoo KH, Jeong K, et al. Thermal oxidation study on lead-free solders of Sn-Ag-Cu and Sn-Ag-Cu-Ge. Adv Eng Mater 2006;8(1-2):111–4.
[168] Wang QM, Gan GS, Du Y, Yang D, Meng G, Wang H, et al. Effect of trace Ge on wettability and high-temperature oxidation resistance of Sn-0.7 Cu lead-free solder. Mater Trans 2016;57(10):1685–90.
[169] Huang N, Hu A, Li M, Mao D. Influence of Cr alloying on the oxidation resistance of Sn–8Zn–3Bi solders. J Mater Sci Mater Electron 2013;24:2812–7.
[170] Xian AP, Gong GL. Oxidation behavior of molten tin doped with phosphorus. J Electron Mater 2007;36:1669–78.
[171] Huang HZ, Wei XQ, Tan DQ, Zhou L. Effects of phosphorus addition on the properties of Sn-9Zn lead-free solder alloy. Int J Miner Metall Mater 2013;20:563–7.
[172] Koyama S, Aoki Y, Shohji I. Effect of formic acid surface modification on bond strength of solid-state bonded interface of tin and copper. Mater Trans 2010;51(10):1759–63.
[173] He S, Gao R, Li J, Shen YA, Nishikawa H. In-situ observation of fluxless soldering of Sn-3.0 Ag-0.5 Cu/Cu under a formic acid atmosphere. Mater Chem Phys 2020;239:122309.
[174] Wang J, Wang Q, Liu Z, Wu Z, Cai J, Wang D. Activation of electroplated-Cu surface via plasma pretreatment for low temperature Cu-Sn bonding in 3D interconnection. Appl Surf Sci 2016;384:200–6.
[175] Lu Q, Chen Z, Zhang W, Hu A, Li M. Low-temperature solid state bonding method based on surface Cu–Ni alloying microcones. Appl Surf Sci 2013;268:368–72.
[176] Geng W, Chen Z, Hu A, Li M. Interfacial morphologies and possible mechanisms of a novel low temperature insertion bonding technology based on micro-nano cones array. Mater Lett 2012;78:72–4.
[177] Peng Y, Tang L, Sun Y, Hu A, Li M. The influence of solder oxidation on low-temperature solid-state bonding based on Ni micro-nano cones. Appl Surf Sci 2023;609:155370.
[178] Sun L, Zhang L, Wei CC, Chen MH, Zhang Y. Transient liquid phase bonding (TLPB) of Cu to Cu using Sn interconnect solder reinforced by submicron Al particles. J Mater Process Technol 2022;307:117686.
[179] Zhang Z, Yang Z, Qu J, Liu Y, Huang J, Chen S, …, Yang J. Magnetron sputtering preparation of Cu6Sn5 preferred-orientation coating and its influence on wettability of Sn-based lead-free solder. Surf Coating Technol 2022;450:129014.
[180] Zhang P, Xue S, Liu L, Wu J, Luo Q, Wang J. Microstructure and shear behaviour of Sn-3.0 Ag-0.5 Cu composite solder pastes enhanced by epoxy resin. Polymers 2022;14(23):5303.
[181] Zhang P, Xue S, Wang J. New challenges of miniaturization of electronic devices: electromigration and thermomigration in lead-free solder joints. Mater Des 2020;192:108726.

[182] Ramli MII, Salleh MM, Yasuda H, Chaiprapa J, Nogita K. The effect of Bi on the microstructure, electrical, wettability and mechanical properties of Sn-0.7 Cu-0.05 Ni alloys for high strength soldering. Mater Des 2020;186:108281.
[183] Huang Y, Xiu Z, Wu G, Tian Y, He P. Sn–3.0 Ag–0.5 Cu nanocomposite solders reinforced by graphene nanosheets. J Mater Sci Mater Electron 2016;27:6809–15.
[184] Xu JQ, Chen LY, Choi H, Li XC. Theoretical study and pathways for nanoparticle capture during solidification of metal melt. J Phys Condens Matter 2012;24(25):255304.
[185] Chen G, Wu F, Liu C, Chan YC. Effect of fullerene-C60&C70 on the microstructure and properties of 96.5 Sn-3Ag-0.5 Cu solder. In 2015 IEEE 65th Electronic Components and Technology Conference (ECTC) 2015, May:1262–7 [IEEE].
[186] Li Y, Xu L, Jing H, Zhao L, Hao K, Han Y. Study on the floating kinetics of graphene in molten Sn-based alloy based on in-situ observation of X-ray radiography. Compos B Eng 2022;238:109909.
[187] Han YD, Yang JH, Xu LY, Jing HY, Lei ZHAO. Effect of transient current bonding on interfacial reaction in Ag-coated graphene Sn–Ag–Cu composite solder joints. Trans Nonferrous Metals Soc China 2021;31(8):2454–67.
[188] Li Y, Xu L, Zhao L, Hao K, Han Y. Shear deformation behavior and failure mechanisms of graphene reinforced Sn-based solder joints bonded by transient current. Mater Des 2022;224:111369.
[189] Liu B, Tian Y, Wang C, An R, Liu Y. Extremely fast formation of CuSn intermetallic compounds in Cu/Sn/Cu system via a micro-resistance spot welding process. J Alloys Compd 2016;687:667–73.
[190] Liu B, Tian Y, Feng J, Wang C. Enhanced shear strength of Cu–Sn intermetallic interconnects with interlocking dendrites under fluxless electric current-assisted bonding process. J Mater Sci 2017;52:1943–54.
[191] Liu HY, Zhu QS, Wang ZG, Guo JD, Shang JK. Effects of Zn addition on electromigration behavior of Sn–1Ag–0.5 Cu solder interconnect. J Mater Sci Mater Electron 2013;24:211–6.
[192] Zhu Z, Sun H, Wu F, Chan YC. Comparative study of the microstructure and mechanical strength of tin-copper (Sn0. 7Cu) solder modified with silver (Ag) by both alloying and doping methods. J Mater Sci Mater Electron 2016;27:6835–44.
[193] Kim Y, Nagao S, Sugahara T, Suganuma K, Ueshima M, Albrecht HJ, ..., Strogies J. Enhanced reliability of Sn–Ag–Bi–In joint under electric current stress by adding Co/Ni elements. J Mater Sci Mater Electron 2014;25:3090–5.
[194] Zhao X, Saka M, Yamashita M, Hokazono H. The effect of adding Ni and Ge microelements on the electromigration resistance of low-Ag based SnAgCu solder. Microsyst Technol 2012;18:2077–84.
[195] Xie HX, Friedman D, Mirpuri K, Chawla N. Electromigration damage characterization in Sn-3.9 Ag-0.7 Cu and Sn-3.9 Ag-0.7 Cu-0.5 Ce solder joints by three-dimensional X-ray tomography and scanning electron microscopy. J Electron Mater 2014;43:33–42.
[196] Shen YA, Lin CM, Li J, Gao R, Nishikawa H. Suppressed growth of (Fe, Cr, Co, Ni, Cu) Sn2 intermetallic compound at interface between Sn-3.0 Ag-0.5 Cu solder and FeCoNiCrCu0. 5 substrate during solid-state aging. Sci Rep 2019;9(1):10210.
[197] Shen YA, Yang XM, Tsai CY, Ouyang YH, Tsai MH, Shun TT. Effect of Cu on the interfacial reaction between Sn-based solders and FeCoNiCu alloys. Intermetallics 2022;144:107530.
[198] Liu X, Chen B, Wu S, Ma Y, Tang S, Wu Z, et al. Growth of the nano-phase intermetallic compounds and its effect on mechanical behavior of Au80Sn20/CrMnFeCoNi solder joints during isothermal aging. J Alloys Compd 2021;859:157823.
[199] Shen YA, Chen SW, Chen HZ, Chang CM, Ouyang YH. Extremely thin interlayer of multi-element intermetallic compound between Sn-based solders and FeCoNiMn high-entropy alloy. Appl Surf Sci 2021;558:149945.
[200] Shen YA, Lin YX, Ouyang FY, Nishikawa H, Tsai MH. Thermomigration suppression in Sn3. 5Ag solder joints by hot-end FeCoNiMn alloy. Intermetallics 2023;154:107821.

Temitope Theophilus Dele-Afolabi: is a lecturer in the Department of Mechanical Engineering, Ajayi Crowther University, Oyo, Nigeria. He is currently working as a Postdoctoral Fellow at the Institute of Power Engineering, Universiti Tenaga Nasional, Jalan Ikram UNITEN, 43000, Kajang, Selangor, Malaysia.

Mohamed Nainar Mohamed Ansari: is an Associate Professor in the Department of Mechanical Engineering, College of Engineering, Universiti Tenaga Nasional, Jalan Ikram UNITEN, 43000, Kajang, Selangor, Malaysia. He is also the head of the Green Energy Materials Group, Institute of Power Engineering, Universiti Tenaga Nasional.

Azmah Hanim binti. Mohamed Ariff: is an Associate Professor in the Department of Mechanical and Manufacturing Engineering, Universiti Putra Malaysia, 43400 UPM Serdang Selangor, Malaysia.

Abdulrahman Adeleke Oyekanmi: is a Postdoctoral Fellow at the Institute of Energy Infrastructure, Universiti Tenaga Nasional, Jalan Ikram UNITEN, 43000, Kajang, Selangor, Malaysia.

Oluwatosin Job Ojo-Kupoluyi: is a Technical Instructor at Nigeria Sugar Institute, Km.18, Ilorin-Kabba Highway, Ilorin, Nigeria.

Atika binti Mohd Afdzaluddin: is a Research Fellow at the Institute of Microengineering and Nanoelectronics, Universiti Kebangsaan Malaysia, 43600 Bangi, Selangor, Malaysia.